In situ ferromagnetic resonance: an ultimate tool to investigate the coupling in ultrathin magnetic films

2003 J. Phys.: Condens. Matter 15 R193

(http://iopscience.iop.org/0953-8984/15/4/204)

INSTITUTE OF PHYSICS PUBLISHING JOURNAL OF PHYSICS: CONDENSED MATTER

J. Phys.: Condens. Matter **15** (2003) R193–R232 PII: S0953-8984(03)37444-2

TOPICAL REVIEW

In situ ferromagnetic resonance: an ultimate tool to investigate the coupling in ultrathin magnetic films

J Lindner and K Baberschke[1]

Institut für Experimentalphysik, Freie Universität Berlin, Arnimallee 14, D-14195 Berlin, Germany

E-mail: bab@physik.fu-berlin.de

Received 6 November 2002
Published 20 January 2003
Online at stacks.iop.org/JPhysCM/15/R193

Abstract

The benefit of using *in situ* ultrahigh vacuum ferromagnetic resonance (FMR) to study exchange coupled magnetic films is demonstrated. Structurally well defined trilayer systems consisting of two ultrathin magnetic films (Ni or Co) separated by a non-magnetic Cu spacer layer are examined. The stepwise construction of the sample reveals how the single uniform resonance mode of the bottom magnetic layer is influenced upon depositing the second layer on top. The coupling leads to an acoustical and an optical mode. The positions, intensities and linewidths of these modes are compared to theory which uses a continuum approach in the framework of the Landau–Lifshitz equation of motion. We discuss how to determine the coupling strength in absolute units which for our trilayers ranges from a few to about 100 μeV/atom and then systematically investigate the parameters that influence this coupling. The effect of the spacer thickness and its roughness is studied in detail with the help of scanning tunnelling microscopy to obtain a realistic and quantitative picture of the spacer morphology. In a next step we investigate the influence of a non-magnetic overlayer usually used as a protection layer. For small coupling strengths such a capping layer can change the sign of the coupling. The temperature dependence of the coupling in the framework of existing theoretical models is discussed. Moreover, the resonance method is used to address via the linewidth the dynamical response of the magnetic layers upon being coupled. It is demonstrated that 2D spin fluctuations originating from one layer influence the damping properties within the other. To support the results obtained from the FMR, the measurements are complemented by magneto-optic Kerr effect experiments on the same systems.

[1] Author to whom any correspondence should be addressed.

Contents

1. Introduction

Since the antiferromagnetic coupling between ferromagnetic films mediated through non-magnetic spacer layers in multilayered structures was discovered [1], a lot of experimental and theoretical effort has been made to understand the basic mechanism on a microscopic scale. The so-called trilayer consisting of only two ferromagnetic films plays an important role, because it is the prototype system to investigate interlayer coupling. Not only is the $T = 0$ ground state of practical and fundamental importance, but also the low $\vec{q}$-vector spin wave spectrum. In contrast to electron excitations and femtosecond spectroscopies, which probe magnetic properties in a hot electron gas, the ferromagnetic resonance (FMR) is the technique of choice [2] to investigate the thermodynamic ground state and its thermal excitations, i.e. low energy spin waves. The effective medium theory can be applied to calculate the excitations in this regime [3]. This approach assumes that the wavelength of the spin wave excitation is long compared to the size of the unit cell within the multilayer, so that the amplitude of the wave is constant over the unit cell. In this limit the paper discusses the various properties that can be derived from FMR experiments on exchange coupled films. Moreover, the advantage of performing the film preparation and the FMR measurements *in situ* is demonstrated. Only then is it possible to measure in a first step the single magnetic film and in a second step after depositing the second magnetic layer the coupled system [4]. In section 2 a brief overview of the theory of interlayer coupling is given and the most frequently used experimental techniques to study such coupling in multilayers are summarized. The dispersion relation of a system of N ultrathin films coupled through non-magnetic spacer layers is derived in section 3. In addition to the fields for resonance we calculate the whole absorption signal for an arbitrary direction of the external magnetic field for an out-of-plane angular dependence. In section 4

we present experimental details concerning the film preparation and magnetic measurements. In section 5 the theoretical predictions for single magnetic films ($N = 1$) as well as for trilayers ($N = 2$) are discussed and compared to our experiments. In particular, we demonstrate how the presence of a coupling field changes the resonance fields and the intensities of the individual magnetic layers. Finally, we show in section 6 how the temperature, the spacer thickness, the spacer roughness and an overlayer influence the coupling. Moreover, the linewidth in coupled systems is addressed.

2. Interlayer coupling in ultrathin magnetic films

Various theoretical approaches used to discuss the observed properties of coupled systems exist, each of them having advantages in describing special features [5]. Most theories focus on the oscillatory character of the coupling as a function of the spacer thickness and successfully explain the observed periods of the oscillatory behaviour. The predictions about the phase and the absolute strength of the interaction are often poorly reproduced in the experiment. Another aspect is the temperature dependence of the coupling for which different models exist [5–7]. Concerning the experimental methods which are used to investigate coupled systems one has to distinguish between the several techniques which only measure a quantity proportional to the coupling and other techniques which can also be used to deduce the absolute value. In the following a brief summary of existing theoretical approaches is given, followed by a comparison of the experimental methods used in the field of coupled ultrathin films.

2.1. Theoretical approaches

Basically two different approaches can be distinguished:

(i) total energy calculations which compute the energy difference between parallel and antiparallel alignment of the neighbouring magnetic layers using either tight-binding or *ab initio* methods and
(ii) model calculations in which a model is applied to characterize the interaction.

Method (i) is usually very complicated, since the energy difference between the two configurations is very small (of the order of 1 meV) compared to the total energy itself, so that numerical convergence of the calculation becomes a problem. As a consequence in most cases only small layer thicknesses are addressed. Model calculations (ii) on the other hand can also be applied to thicker films and in most cases end in analytical results. Therefore, they give transparent physical pictures which numerical total-energy calculations often do not provide. Several models have been used. The most popular ones are the following.

(i) The Ruderman–Kittel–Kasuya–Yosida (RKKY) model, which was originally developed by Ruderman and Kittel [8] to explain the interaction of nuclear magnetic moments mediated by conduction electrons. Kasuya [9] and Yosida [10] extended it to the case of electronic magnetic moments. In the RKKY framework the magnetic layers are described by localized spins. Spin $\vec{S}_n^i$ located at site $\vec{R}_n$ in magnetic layer i interacts via a contact potential $U = A\delta(\vec{r} - \vec{R}_n)\vec{s} \cdot \vec{S}_n^i$ with a conduction electron in the spacer with spin $\vec{s}$ located at position $\vec{r}$. The parameter A describes the strength of the coupling. Using second order perturbation theory the effective interaction between the spins $\vec{S}_n^i$ and $\vec{S}_m^{i+1}$ of adjacent magnetic layers i and $i + 1$ can be written as $U_{n,m} = J_{n,m}\vec{S}_n^i \cdot \vec{S}_m^{i+1}$. This expression has the same form as the Heisenberg exchange between two spins in *one* magnetic film, but $J_{n,m}$ has to be distinguished from the temperature independent exchange integral of the Heisenberg interaction. Summing up all $J_{n,m}$-values one gets the interaction energy of

two adjacent layers $J_{inter}^{n,m}$. In addition, for single-domain films (see section 3.1) all spins are aligned almost parallel and the spins sum up to uniform magnetization vectors $\vec{M}_n$ and $\vec{M}_m$. Then, the total energy of the coupled system due to the coupling may be written as $U_{ex} = J_{inter}^{n,m}\,\vec{M}_n \cdot \vec{M}_m$ and $J_{inter}^{n,m}$ now describes the energy difference between parallel and antiparallel alignment of the two magnetization vectors.

(ii) The sd-mixing model using an Anderson Hamiltonian [11]. Within a Friedel–Anderson picture this method was developed to describe the coupling of magnetic impurities in dilute alloys where the localized energy states of the impurity are broadened by hybridization with the conduction electrons of the host material (sd mixing) which induces an oscillatory spin polarization around the impurity. The advantage of this approach is the more realistic treatment of the interaction between the localized states and the conduction electrons compared to e.g. the interaction via a contact potential used in RKKY methods. Therefore, the strength and the phase of the oscillatory coupling can be predicted in a much better way. However, the calculations are more complicated and physically less transparent.

(iii) The hole confinement model [12], where spin dependent potential steps are introduced at the interfaces of the spacer to the ferromagnets.

A detailed overview over models (i)–(iii) is given in the work of Bruno [5] and references therein. Despite the different approaches a lot of predictions are supported by all models. The most important results concerning this paper will be discussed separately for $T = 0$ and for $T \neq 0$ in the following sections.

2.1.1. $T = 0$. At $T = 0$ one can write the coupling as

$$\frac{J_{inter}}{J_{inter,0}} \sim \frac{1}{d^2} \sum_j \sin(k_j^s d + \phi_j). \tag{1}$$

Here $J_{inter,0}$ is the value of J_{inter} at $T = 0$, the k_j^s give the oscillation periods, ϕ_j are the phases and d is the spacer thickness. Due to its discrete nature the spacer thickness can only be a multiple of the interlayer spacing d_{inter}, i.e. $d = (l + 1)\, d_{inter}$ where l is the number of atomic layers. In the following we use the term monolayer (ML) for $d = 1\, d_{inter}$. Equation (1) shows that the oscillation periods of the coupling depend only on the characteristics of the Fermi surface of the spacer material. They are given by extremal spanning vectors of the Fermi surface k_j^s [5, 13, 14]. In particular, the number of periods increases as the in-plane density of the spacer-atoms decreases [5]. This is observed in experiments for Cu spacers, where a single period is found for the (111)-, two periods for the (001)- and three for the (110)-orientation. The two predicted periods for Cu(001), the spacer material throughout this paper, are 2.56 and 5.88 ML. The intensities and phases ϕ_j depend on the Fermi surface characteristics of the spacer as well, but also on the interaction between the conduction electrons in the spacer and the spins in the magnetic layers [5, 11]. Therefore, to predict strength and phase a realistic interaction potential including real band-structures must be taken into account.

2.1.2. $T \neq 0$. Basically two different mechanisms exist to explain the temperature dependence of the interlayer coupling.

(i) Thermally excited spin waves in the magnetic layers lead to a reduction of the effective interlayer exchange [6]. In this model the characteristic quantity influencing the temperature dependence is given by T_C, and J_{inter} as a function of T is

$$\frac{J_{inter}}{J_{inter,0}} = 1 - a\left(\frac{T}{T_C}\right)^{3/2} \tag{2}$$

where a is of order unity [6].

(ii) Thermal excitations of electron–hole pairs across the Fermi level in the spacer material [5, 7]. These excitations are described by the rounding of the Fermi–Dirac distribution function at elevated temperatures which leads to a decrease of the effective coupling between the magnetic layers given by J_{inter}

$$\frac{J_{inter}}{J_{inter,0}} = \frac{T/T_0}{\sinh(T/T_0)} \tag{3}$$

where $T_0 = (\hbar v_F)/(2\pi k_B d)$ is the value which determines the functional behaviour. v_F, the only temperature dependent quantity within T_0, is the Fermi velocity of the carriers in the spacer with thickness d. In this model the coupling does not necessarily vanish at the Curie temperature T_C. Large Fermi velocities v_F, i.e. large T_0-values, decrease the effective temperature dependence. In particular, for noble metal spacers v_F is quite large (about 10^8 cm s^{-1}) so that only a small temperature dependence in the range 1–1000 K can be expected. Another quantity which does not explicitly enter model (i) is d. According to model (ii) larger spacer thicknesses lead to a more pronounced temperature dependence. Both models will be compared with experimental results in section 6.1.

2.2. Comparison of various experimental techniques used to investigate coupled magnetic films

When discussing the techniques that can be used to investigate coupled ultrathin films, one has to distinguish between

(i) magnetometry methods which are sensitive to the static magnetization and
(ii) others which measure the dynamical response of a magnetic system, i.e. spin wave excitations.

Methods of category (i): common to all techniques within (i) is that they deduce the coupling from measurements of the absolute magnetization or a quantity being proportional to it. There exist several kinds of magnetometer like the alternating gradient magnetometer (AGM), the vibrating sample magnetometer (VSM), the torsion oscillation magnetometer (TOM) or magnetometers using superconducting quantum interference devices (SQUIDs) which all measure the magnetization in absolute units. Some of these techniques have been combined with ultrahigh vacuum (UHV) systems [15]. The magneto-optic Kerr effect (MOKE) which is sensitive down to the submonolayer regime is one of the most commonly used methods under UHV conditions. The Kerr signals are, however, only proportional to the magnetization, so that one has to calibrate the system with a known bulk sample each time a new specimen is investigated. Usually, magnetometries deduce the coupling from field dependent measurements of the magnetization, i.e. via the analysis of hysteresis loops. For antiferromagnetic coupling the switching field needed to align the magnetizations parallel to each other is a direct and absolute measure of the coupling. However, this is only true if all other parameters determining the hysteresis loop are either known or much smaller than the coupling energy given by J_{inter}. Therefore, magnetic anisotropies usually complicate the analysis of hysteresis loops, because they have to be determined simultaneously with J_{inter}. For ferromagnetically coupled films, despite the sign, usually no absolute value of the coupling can be determined, since for this case all magnetizations are aligned parallel even at remanence. Such systems can be addressed only in special cases via the introduction of additional magnetic layers which pin one of the two ferromagnetically coupled layers via a stronger antiferromagnetic coupling. Finally, x-ray magnetic circular dichroism (XMCD) should be mentioned. Again calibrating parameters are necessary to deduce the magnetic

moments, but this technique offers the unique possibility to separate the contributions to the magnetization within a sample due to its element specificity. In addition, it allows for several systems to separate the spin and orbital contribution to the magnetic moment via the 'sum-rules'. XMCD is able to deduce values for ferro- and antiferromagnetically coupled systems. It provides, however, only a relative value for the coupling strength [16].

Methods of category (ii): concerning the possibility of absolute magnetometry techniques like FMR, Brillouin light-scattering (BLS) or inelastic neutron scattering are only capable of deducing relative values for the static magnetization which can be calibrated to bulk samples. Besides this the latter techniques give access to the spin wave spectrum which all the methods mentioned up to now do not. In particular, FMR and BLS allow us to determine anisotropies very precisely and, moreover, to separate the several contributions to the overall anisotropy which from Kerr effect measurements or other static magnetometries is often not possible. Compared to FMR the BLS results are usually less precise because the frequency resolution of a typical BLS experiment is only about 300 MHz, whereas in an FMR measurement the resolution is given by the linewidth of the signal being in the range of 30 MHz. After the effect of interlayer exchange coupling was discovered, a rather new field for FMR and BLS was created, where both were also shown to be powerful tools [1, 17, 18, 20–23]. They provide the coupling strength in absolute units for ferro- as well as for antiferromagnetically coupled films, whereas techniques like the MOKE or magneto-resistance measurements usually only give access to antiferromagnetic coupling (see above). Thus, by using FMR or BLS, one can measure the anisotropies and the coupling independently from each other. If the measurements are performed *in situ* in UHV, the separation of the several parameters are even more direct, as will be shown by our FMR experiments. FMR, BLS and inelastic neutron scattering are complementary methods, since the difference between the three techniques lies in the range of the wavevectors of the probed spin wave modes. FMR probes spin wave excitations with the wavevector $q = 0$, i.e. excitations close to the centre of the Brillouin zone. Such modes are called uniform, because all spins precess in phase. These modes are the ground states corresponding to the thermal excitations, kT. BLS on the other hand excites spin wave modes corresponding to the energy $\hbar\omega$ and momentum of the incident light. Such modes are strongly influenced by the intralayer exchange forces because the spins now present phase shifts with respect to each other. For some cases it is also possible in FMR experiments to excite modes having $q \neq 0$. These modes are called magnetostatic because they have large wavelengths of the order of the sample size, so that they are governed mainly by dipolar forces. It is important to note that all the modes which can be addressed with FMR are non-propagating (one example is the standing spin waves seen in micrometre films). Inelastic neutron scattering allows us to probe q-values within the whole Brillouin zone; however, it is not usually sensitive enough to measure down to film thicknesses of only a few atomic layers. Table 1 summarizes all features of the different experimental methods.

Now we turn to the details of the FMR spectroscopy which is among the established techniques to determine principal parameters of magnetic systems. Besides magnetic anisotropies [2] the g-value, usually a tensor quantity in solids, is a rather important one of these parameters [24].

Figure 1 shows the Zeeman splitting of a twofold degenerate energy level by $\vec{H}_0$. A microwave field $\vec{h}_{rf}$ with frequency f which is coupled into the cavity at right angles to the static field will induce transitions between the two levels N_1 and N_2. The spin system will absorb microwave power and thus produce an FMR signal if $hf = g\mu_B H_{res}$, H_{res} being the resonance field. With the gyromagnetic ratio $\gamma = g\mu_B/\hbar$ ($\gamma/2\pi = 2.8\,\mathrm{GHz\,kOe^{-1}}$ for $g = 2$) one can write this resonance condition as $2\pi f = \gamma H_{res}$. The frequency of the microwave typically lies in the gigahertz range. Consequently, the energy transfer is small leading to

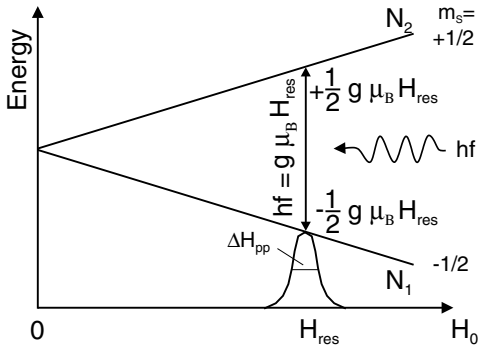

Figure 1. Schematic diagram of ferromagnetic (paramagnetic) resonance.

Table 1. Comparison between different experimental methods to investigate ferromagnetic (FM) and antiferromagnetic (AFM) coupled films. q is the wavevector of the probed spin waves.

		Measure of J_{inter}		
Method	Magnetometry	AFM	FM	Spin wave dispersion
MOKE	Relative	Absolute	Relative	No
XMCD	Relative	Relative	Relative	No
SQUID, VSM, AGM, TOM	Absolute	Absolute	Relative	No
BLS	Relative	Absolute	Absolute	$q \approx 1 \times 10^7$ m^{-1}
FMR	Relative	Absolute	Absolute	$q \approx 0$

a high resolution within an FMR experiment. The FMR signal provides three quantities: H_{res}, the linewidth ΔH_{pp} and the resonance intensity I, being the integral of the absorption signal. The analysis of ΔH_{pp} allows us to study magnetic relaxation processes [25]. I is a measure of the sample magnetization [18]. The number of magnetic moments which are still detectable is of the order of 10^{10}–10^{14}. This corresponds to film thicknesses of 1–10^4 ML on a 1 cm^2 sample and shows that the sensitivity of FMR allows us to investigate bulk samples as well as systems down to film thicknesses of a single atomic layer. Because of the large quantum numbers involved in the transition between N_1 and N_2 one can use a classical picture to describe the resonance phenomenon. Due to the presence of $\vec{H}_0$ the spins within the sample will precess about the field direction with the Larmor frequency f_L. This precession produces an oscillatory magnetic moment normal to the static field, so that an external microwave field $\vec{h}_{rf}$ of frequency f_L perpendicular to the static field produces magnetic dipole transitions M1. Instead of varying the frequency, in most cases a fixed frequency f is used and the resonance is achieved by increasing the static field H_0. In the following we show how FMR is used to investigate coupled ferromagnetic layers and what detailed information can be obtained.

3. Ferromagnetic resonance in exchange coupled films

3.1. Dynamical equation of motion in the ultrathin film limit

Two methods have been applied to analyse FMR in coupled films:

(i) the energy method introduced by Smit and Beljers [26] and
(ii) the vectorial formalism given by the LL equation of motion [27].

Method (i) was used in [20, 22, 23]; it simplifies the mathematical apparatus compared to (ii). It has the disadvantage that only the mode positions (resonance fields) are obtained. The intensities and the linewidths of the modes, i.e. the whole resonance signal, can be deduced additionally in the LL formalism. We apply the LL equation of motion within this paper. For a single magnetic moment $\vec{\mu}_n$ arising from a spin $\vec{S}_n$ located at the site of the nth atom in a magnetic specimen, the LL equation is written as

$$-\frac{1}{\gamma}\frac{\mathrm{d}\vec{\mu}_n}{\mathrm{d}t} = \vec{\mu}_n \times \left(\vec{H}^{eff}_{\mu_n} + \vec{H}_0 + \vec{h}^{rf}_{\mu_n}\right). \tag{4}$$

$\vec{H}^{eff}_{\mu_n}$ is the effective internal magnetic field inside the sample, which is added to the external one $\vec{H}_0$. $\vec{h}^{rf}_{\mu_n}$ is the high frequency magnetic field generated by the microwaves at the position of the magnetic moment. The expression on the right-hand side of equation (4) is the torque acting on the atomic moment $\vec{\mu}_n$. In general one starts to calculate the FMR signal by combining equation (4) with Maxwell's equations for the electric and magnetic fields within the sample Then one solves a boundary problem appropriate for the experimental geometry. To find such a solution for a film of arbitrary thickness is very difficult. However, the calculation of the lineshape can be simplified for the case of an ultrathin film, i.e. when the film thickness is small compared to the exchange length $L_{exch} = \sqrt{A/2\pi M_S^2}$ and the skin depth $L_{skin} = c/\sqrt{2\pi\mu\omega\sigma}$. Here A is the exchange stiffness, M_S the saturation magnetization, μ the magnetic permeability, ω the circular microwave frequency and σ the conductivity. The first condition implies that the strong exchange interactions keep all magnetic moments parallel across the specimen, so that the film can be regarded as a giant molecule. The second condition causes the electric and magnetic fields to be constant across the sample. For Ni, Co and Fe one has $L_{exch} \approx 30$–70 Å and $L_{skin} \approx 300$ Å at a frequency of 9 GHz. Since the thicknesses of the magnetic layers within this paper are less than 20 Å, our films can be considered as ultrathin. Therefore, all moments in equation (4) are summed up across the film thickness. With $\vec{\mu}_t = \sum \vec{\mu}_n$ being the total magnetic moment, equation (4) becomes

$$\frac{\mathrm{d}\vec{\mu}_t}{\mathrm{d}t} = -\gamma\left(\vec{\mu}_t \times \sum_n \frac{\mu_n}{\mu_t}\vec{H}^{eff}_{\mu_n} + \vec{H}_0 + \vec{h}_{rf}\right). \tag{5}$$

The term on the right-hand side defines the macroscopic effective field $\vec{H}^{eff} = \sum_n \frac{\mu_n}{\mu_t}\vec{H}^{eff}_{\mu_n}$ and represents the overall internal magnetic field acting upon the total moment $\vec{\mu}_t$. $\vec{h}_{rf}$ is constant over the sample. Considering the macroscopic magnetization $\vec{M} = \vec{\mu}_t/V$ (V is sample volume), the macroscopic equation of motion can be written as

$$\frac{\mathrm{d}\vec{M}}{\mathrm{d}t} = -\gamma\vec{M} \times \left(\vec{H}^{eff} + \vec{H}_0 + \vec{h}_{rf}\right). \tag{6}$$

For diluted paramagnetic samples $\vec{H}^{eff} = 0$, so that the torque is only produced by the external magnetic field $\vec{H}_0$. In a ferromagnet, however, internal fields have to be added.

3.2. Dispersion relation for N ultrathin magnetic films

Now the dispersion relation for a layered structure consisting of N magnetic layers separated by non-magnetic spacer layers (see figure 2) is derived. In this scheme the trilayer for $N = 2$ can be considered as the prototype. The following assumptions are made within our model.

(i) All layers are ultrathin, so that one can apply the LL equation of motion, equation (6). This is equal to assuming that only the lowest order spin-wave mode across each magnetic layer is excited. To excite higher order spin-wave modes with $q_\perp \neq 0$ in ultrathin films much larger external magnetic fields ($>10^3$ kOe) are needed.

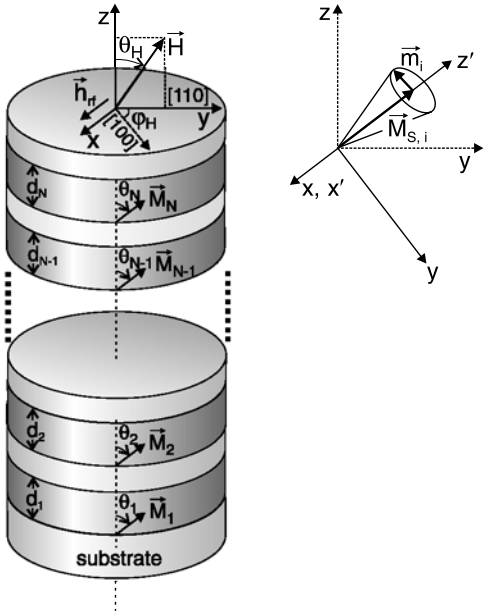

Figure 2. Coordinate system used to describe the N exchange coupled ultrathin films. $\theta_{H/i}$ ($\varphi_{H/i}$) corresponds to the polar (azimuthal) orientation of $\vec{H}_0$ and $\vec{M}_i$ with $i = 1, \ldots, N$.

(ii) A uniform microwave field $\vec{h}_{rf}$ across the film plane is assumed. This implies that no spatial variation *parallel* to the film plane occurs or, in other words, spin-wave modes having an in-plane wavevector $q_\parallel \neq 0$ are not excited.
(i) and (ii) only allow the uniform precession ($q_\parallel = q_\perp = 0$) within the layers.

(iii) Because $q_\parallel = 0$ the dipole–dipole interaction between two magnetic layers vanishes, since only for $q_\parallel \neq 0$ would the motion of the spins produce stray fields which leak out of the films and subsequently couple the films through dipolar forces.

Therefore, $q_\parallel = 0$ implies that *only* exchange interactions produce a coupling between the layers. Here exchange interaction has to be understood in the framework of the discussion in section 2.1. This interlayer exchange is considered to be equivalent to an extra torque acting on the surface spins of each magnetic layer and can be replaced by an effective exchange field which is introduced in the LL equation of motion. Thus, the coupling acts on the layer like an extra magnetic field which for ultrathin films can be assumed to be uniform.

Figure 2 shows the coordinate system which is appropriate for our experimental geometry. The magnetic films with thicknesses d_i lie in the x/y-plane with x and y being the $[1\bar{1}0]$- and the [110]-direction, respectively. They have magnetizations $\vec{M}_i$ forming an angle θ_i with the z-axis, being the film normal. The in-plane angles φ_i are measured with respect to the in-plane [100]-direction. The external magnetic field $\vec{H}_0$ can be continuously rotated in the y/z-plane given by the angle θ_H measured with respect to the z-axis. The microwave field $\vec{h}_{rf}$ oscillates along the x-direction. Only small deviations from the equilibrium positions are considered or, in other words, $h_{rf} \ll H_0$. Then, in equilibrium $\vec{M}_i = \vec{M}_{S,i}$, where $\vec{M}_{S,i}$ are the saturation magnetization values. In this section we assume that due to the presence of the external field $\vec{H}_0$ all the $\vec{M}_i$ are restricted to the y/z-plane. This restriction can be dropped in our calculations without problems, but it allows us to keep the calculations simple and illustrative. Other cases (e.g. the one where the magnetizations are restricted to the film plane) can be treated in analogy

to the case presented here. In addition, the restriction is appropriate for most of the systems investigated in this paper, because they have an in-plane easy axis along the [110]-direction (y-axis).

The first step is to calculate the equilibrium positions θ_i^0 of the magnetizations $\vec{M}_i$ in each film i for a given external field. For this the total free energy density F per unit area has to be a minimum, i.e. the θ_i^0-values are given by the set of N coupled equations

$$\frac{\partial F}{\partial \theta_i} = 0 \tag{7}$$

from which the equilibrium angles for the general case have to be determined numerically. It should be noted that, upon knowing the θ_i^0-values, one can already calculate the overall magnetization component along the direction of the applied field $\vec{H}_0$ by adding all contributions of the individual films

$$\frac{M(H_0)}{M_S} = \frac{\sum_{i=1}^{N} M_i \cos(\theta_i^0 - \theta_H)}{\sum_{i=1}^{N} M_i}. \tag{8}$$

This formula can be used as a *simple* approach to analyse Kerr-effect measurements, but since it is assumed that the system always approaches its equilibrium, no hysteresis effects can be modelled. To calculate the dynamical response which one needs to analyse the FMR absorption signal, the time dependent components of the magnetization vectors have to be evaluated. F can be written as

$$F = \sum_{i=1}^{N} U_{Z,i} + U_i. \tag{9}$$

Here $U_{Z,i} = -d_i \vec{M}_i \cdot \vec{H}_0$ is the Zeeman energy per unit area

$$U_{Z,i} = -d_i M_i H_0 \cos(\theta_i - \theta_H) = -d_i M_i H_0 (\cos\theta_H \cos\theta_i + \sin\theta_H \sin\theta_i). \tag{10}$$

U_i is the internal total energy density in the magnetic layers. For our systems three basic contributions within U_i are considered:

$$U_i = U_{A,i} + U_{dip,i} + U_{ex,i}. \tag{11}$$

$U_{A,i}$ is the anisotropy energy density. The thin films which are investigated throughout this paper are tetragonally distorted due to their pseudomorphic growth upon the substrate. Thus, a non-zero second order perpendicular uniaxial anisotropy term K_2 is created by the vertical lattice distortion. The in-plane and out-of-plane axes are now inequivalent, so that the term K_4 will split into a fourfold in-plane term $K_{4\parallel}$ and a fourfold perpendicular term $K_{4\perp}$. Therefore, the anisotropy energy for *one* tetragonally distorted film has to be written as $U_A \propto -K_2\alpha_z^2 - \frac{1}{2}K_{4\parallel}(\alpha_x^2+\alpha_y^2) - \frac{1}{2}K_{4\perp}\alpha_z^2$. Here α_x, α_y and α_z are the direction cosines of the $\vec{M}_i$ with respect to the cubic [100], [010] and [001] crystallographic axes [2]. We will, however, show that for the special thickness range of our films, the K_4-terms are smaller by at least a factor of ten than the uniaxial K_2-term. In general the K_4-terms cannot be neglected [2]. By leaving only the uniaxial terms, which may be written as uniaxial anisotropy fields $H_{u,i} = 2K_{2,i}/M_i$, and by taking into account that for our coordinate system $\alpha_{z,i}^2 = M_{z,i}^2/M_i^2 = \cos^2\theta_i$, one can write $U_{A,i}$ in a similar form to the Zeeman term

$$U_{A,i} = -d_i M_i \tfrac{1}{2} H_{u,i} \cos^2\theta_i. \tag{12}$$

In our notation $H_{u,i} > 0$ indicates a preferential direction of the $\vec{M}_i$ along the uniaxial axis, whereas $H_{u,i} < 0$ leads to an energy minimum for $\vec{M}_i$ in the film plane. $U_{dip,i}$ is the demagnetizing energy

$$U_{dip,i} = d_i 2\pi M_{z,i}^2 = -d_i M_i \tfrac{1}{2} H_{dip,i} \cos^2\theta_i. \tag{13}$$

$H_{dip,i} = -4\pi M_i$ are the demagnetizing fields of the layers resulting from the magnetic charge density that develops if the magnetizations are rotated out of the film plane. As a consequence $U_{dip,i}$ always has its minimum for $\vec{M}_i$ lying in the film plane. The resonance position is determined by the sum of $H_{dip,i}$ and $H_{u,i}$. Therefore, it is useful to introduce the effective magnetization $M_{eff,i} = 2K_{2,i}/M_i - 4\pi M_i$. A negative value of $M_{eff,i}$ indicates an easy axis in the film plane, whereas a positive one shows an easy axis along the film normal.

Finally, $U_{ex,i}$ is the interlayer exchange coupling energy of layer i arising from the interaction with the neighbouring layers $i-1$ and $i+1$ as introduced in section 2.1

$$U_{ex,i} = -J_{inter}^{i,i-1}\frac{\vec{M}_i \cdot \vec{M}_{i-1}}{M_i M_{i-1}} - J_{inter}^{i,i+1}\frac{\vec{M}_i \cdot \vec{M}_{i+1}}{M_i M_{i+1}}. \tag{14}$$

Here $J_{inter}^{i,i-1}$ and $J_{inter}^{i,i+1}$ are the bilinear interlayer exchange coupling constants between film i and $i-1$ and i and $i+1$, respectively. Positive values of J_{inter} indicate ferromagnetic coupling whereas negative ones antiferromagnetic coupling. As discussed in section 2.1 J_{inter} is a measure of the energy, normalized to a unit area, between the parallel and the antiparallel state of the two magnetizations. It would be possible to introduce higher order terms of the coupling like the biquadratic coupling which favours a 90° alignment of the two $\vec{M}_i$. Such a coupling has been observed e.g. in Fe/Cr/Fe structures, where it was shown to be quite strong, reaching values even comparable to J_{inter} [23]. For our systems, however, the biquadratic term plays a negligible role. At this point the role of exchange fields *within* the layers, i.e. intralayer exchange fields, shall be discussed. A spatial variation of the precessing angles of the spins inside the magnetic layers would create intralayer exchange torques which alter the resonance condition. As discussed above (section 3.1), for ultrathin films such variations give only a negligibly small correction to the resonance condition [18].

To continue the calculation one introduces a new Cartesian coordinate system which is obtained from the $x/y/z$-system of figure 2 by rotation about the x-axis, so that the z'-axis coincides with the time independent saturation magnetization $\vec{M}_{S,i}$ as shown in the inset of figure 2. Then, the new x'-axis coincides with the x-axis. Due to the high frequency microwave field the total magnetization $\vec{M}_i$ precesses around the z'-axis. When $\vec{m}_i(t) = (m_{x',i}, m_{y',i}, 0)$ denotes the time dependent contribution to $\vec{M}_i$, $\vec{M}_i(t)$ can be written in the $x'/y'/z'$-system as

$$\vec{M}_i(t) = (m_{x',i}(t), m_{y',i}(t), M_{S,i}). \tag{15}$$

The transformation from the original variables is given by

$$\begin{aligned} M_{x,i}(t) &= m_{x',i}(t) \\ M_{y,i}(t) &= m_{y',i}(t)\cos\theta_i + M_{S,i}\sin\theta_i \\ M_{z,i}(t) &= -m_{y',i}(t)\sin\theta_i + M_{S,i}\cos\theta_i. \end{aligned} \tag{16}$$

In the same way as the magnetizations, the effective fields within the layers in the $x'/y'/z'$-system become

$$\vec{H}_i^{eff}(t) = \left(H_{x',i}^{eff}(t), H_{y',i}^{eff}(t), H_{z',i}^{eff}(t)\right). \tag{17}$$

$\vec{H}_i^{eff}$, needed for the LL equation of motion, is related to U_i by

$$H_{\alpha,i}^{eff} = -\frac{1}{d_i}\frac{\partial U_i}{\partial M_{\alpha,i}}\bigg|_{\theta_i=\theta_i^0}, \qquad \alpha = x', y', z'. \tag{18}$$

By using equations (11), (16) and (18) the components of the effective field are

$$\begin{aligned} H_{x',i}^{eff}(t) &= J_{inter}^{i,i-1}\frac{m_{x',i-1}(t)}{M_{S,i-1}M_{S,i}d_i} + J_{inter}^{i,i+1}\frac{m_{x',i+1}(t)}{M_{S,i+1}M_{S,i}d_i} \\ H_{y',i}^{eff}(t) &= a_0 m_{y',i-1}(t) + b_0 m_{y',i}(t) + c_0 m_{y',i+1}(t) + d_0 M_{S,i-1} - e_0 M_{S,i} + f_0 M_{S,i+1} \\ H_{z',i}^{eff}(t) &= -d_0 m_{y',i-1}(t) - e_0 m_{y',i}(t) - f_0 m_{y',i+1}(t) + a_0 M_{S,i-1} + b_0 M_{S,i} + c_0 M_{S,i+1}. \end{aligned} \tag{19}$$

Here

$$\begin{aligned} a_0 &= J_{inter}^{i,i-1}\frac{\cos(\theta_{i-1}^0-\theta_i^0)}{M_{S,i-1}M_{S,i}d_i}, & b_0 &= M_{eff,i}\frac{\sin^2\theta_i^0}{M_{S,i}} \\ c_0 &= J_{inter}^{i,i+1}\frac{\cos(\theta_{i+1}^0-\theta_i^0)}{M_{S,i+1}M_{S,i}d_i}, & d_0 &= J_{inter}^{i,i-1}\frac{\sin(\theta_{i-1}^0-\theta_i^0)}{M_{S,i-1}M_{S,i}d_i} \\ e_0 &= M_{eff,i}\frac{\sin 2\theta_i^0}{2M_{S,i}}, & f_0 &= J_{inter}^{i,i+1}\frac{\sin(\theta_{i+1}^0-\theta_i^0)}{M_{S,i+1}M_{S,i}d_i}. \end{aligned} \tag{20}$$

Inserting equation (19) into the LL equation of motion (equation (6)), assuming an $e^{i\omega t}$-dependence for $\vec{m}_i(t)$ and substituting for the derivatives provides

$$\begin{aligned} &b_1 m_{y',i-1} + c_1 m_{x',i} + d_1 m_{y',i} + f_1 m_{y',i+1} = 0 \\ &a_2 m_{x',i-1} + c_2 m_{x',i} + d_2 m_{y',i} + e_2 m_{x',i+1} = M_{S,i} h_{rf,x} \end{aligned} \tag{21}$$

where

$$\begin{aligned} c_1 &= d_2 = -\frac{i\omega}{\gamma}, \qquad b_1 = -a_2 = f_1 = -e_2 = \frac{J_{inter}}{M_S d}, \\ c_2 &= \frac{2J_{inter}}{M_S d} + M_{eff,i}\cos^2\theta_i^0 + H_0\cos(\theta_i^0-\theta_H), \\ d_1 &= -\frac{2J_{inter}}{M_S d} - M_{eff,i}\cos 2\theta_i^0 - H_0\cos(\theta_i^0-\theta_H). \end{aligned} \tag{22}$$

Equation (21) describes a $2N \times 2N$ system of equations from which the $m_{x',i}$ and $m_{y',i}$ and then, via equation (15), $\vec{M}_i(t)$ can be calculated. The transformation of the components of $\vec{M}_i$ into the $x/y/z$-system is done with the help of equation (16). The FMR absorption signal, i.e. the absorbed microwave power P, can then be obtained by

$$P \propto \sum_{i=1}^{N} \mathrm{Re}\left(h_{rf,x}^* \frac{\mathrm{d}m_{x',i}}{\mathrm{d}t}\right). \tag{23}$$

Taking into account that $h_{rf,x}$, $m_{x',i} \propto \exp(i\omega t)$, one can also write in the more commonly used form

$$P \propto \omega h_{rf,x}^2 \sum_{i=1}^{N} \mathrm{Im}\left(\frac{m_{x',i}}{h_{rf,x}}\right) \tag{24}$$

with $\chi_{x',i} = m_{x',i}/h_{rf,x}$ the component of the high frequency susceptibility along the microwave field[2].

Before applying the results to our experiment, the explicit expressions for the cases of a single film ($N = 1$) and the trilayer ($N = 2$) are given. For the single film equation (21) reduces with $\theta_1^0 := \theta$ to

$$\begin{aligned} &\frac{i\omega}{\gamma} m_{x'} + [H_0\cos(\theta-\theta_H) + M_{eff}\cos 2\theta] m_{y'} = 0 \\ &[H_0\cos(\theta-\theta_H) + M_{eff}\cos^2\theta] m_{x'} - \frac{i\omega}{\gamma} m_{y'} = M_S h_{rf,x}. \end{aligned} \tag{25}$$

For the trilayer one calculates from equation (21)

$$\begin{aligned} &c_1 m_{x',i} + d_1 m_{y',i} + f_1 m_{y',i+1} = 0 \\ &c_2 m_{x',i} + d_2 m_{y',i} + e_2 m_{x',i+1} = M_{S,i} h_{rf,x}. \end{aligned} \tag{26}$$

[2] One should note that in order to keep the presentation more illustrative no damping term has been considered in the equation of motion (equation (6)). Therefore, $\chi_{x',i}$ has no imaginary part, i.e. no energy dissipation takes place. Consequently, no microwave power is absorbed in the sample, so that $P = 0$ in equation (24). Strictly speaking, equation (21) can only be used to calculate resonance fields. Damping will be considered in section 6.2.

3.3. Single film

In the following, we will discuss the FMR resonance field for a single film. We calculate $f(H_0)$ for various angles of the external field, using realistic values for the magnetization and anisotropy of the film.

Taking into account that $x = x'$ one can deduce the rf susceptibility $\chi_x = m_x/h_{rf,x}$ from equation (25)

$$\chi_x = \frac{M_S[H_0\cos(\theta-\theta_H)+M_{eff}\cos(2\theta)]}{[H_0\cos(\theta-\theta_H)+M_{eff}\cos^2\theta][H_0\cos(\theta-\theta_H)+M_{eff}\cos 2\theta]-\left(\frac{\omega^2}{\gamma^2}\right)}. \tag{27}$$

This equation can be used to simulate FMR signals for single films and for an arbitrary angle θ_H of the magnetic field, when it is inserted into equation (24). To simulate the whole FMR line, however, damping has to be included as shown (e.g. [18]). The resonance condition is obtained by setting the denominator equal to zero

$$\left(\frac{\omega}{\gamma}\right)^2 = [H_0\cos(\theta-\theta_H)+M_{eff}\cos^2\theta][H_0\cos(\theta-\theta_H)+M_{eff}\cos 2\theta]. \tag{28}$$

The changes to the resonance condition when K_4-terms and/or a rotation of the external field $\vec{H}_0$ within the film plane is included are discussed in [2]. From the resonance condition the resonance field is obtained, and therefore equation (28) can be used to fit angular dependent FMR measurements, once the equilibrium angle θ of the magnetization has been determined from equation (7). For the special cases where the external field is applied in the film plane ($\theta_H = 90°$) which, in addition, is the easy axis of magnetization ($\theta = 90°$), equation (28) reduces to

$$\left(\frac{\omega}{\gamma}\right)^2 = H_0[H_0 - M_{eff}]. \tag{29}$$

If the external field is applied along the film normal ($\theta_H = 0°$), which is an easy axis ($\theta = 0°$), equation (28) yields

$$\left(\frac{\omega}{\gamma}\right) = H_0 + M_{eff}. \tag{30}$$

If one does not measure along an easy axis, the internal field is not parallel to the external one. Equation (7) may then result in two energy minima. One minimum occurs for field values which are large compared to the internal fields. In this case the external field and the magnetization are parallel. The other minimum occurs for field values which are smaller than the internal fields. Now the magnetization is not parallel to the external field so that, at resonance, the magnetization precesses about the internal field direction. Figure 3 shows the resonance frequency as a function of the external field for a system with easy axis out of plane (left-hand panel) and one having an easy axis in plane (right-hand panel) as predicted by equation (28). The figure illustrates the difference between measuring along an easy and a hard axis for the two cases. The angle θ_H of the external field according to figure 2 is given as a parameter. A film with magnetization of $M = 0.485$ kG (value of bulk Ni at room temperature) has been assumed. Furthermore, no in-plane anisotropy is considered, since we focus on the out-of-plane angular dependence, i.e. the external field $\vec{H}_0$ is rotated only within the y/z-plane (see figure 2). Since the shape anisotropy $2\pi M_z^2$ already creates an easy axis within the isotropic film plane ($\theta = 90°$), no intrinsic out-of-plane anisotropy given by K_2 is needed for an easy in-plane system and was therefore neglected in the right-hand panel of figure 3. To create an easy axis along the film normal, however, one needs an out-of-plane anisotropy which overcomes the shape anisotropy, i.e. M_{eff} has to become positive. In the

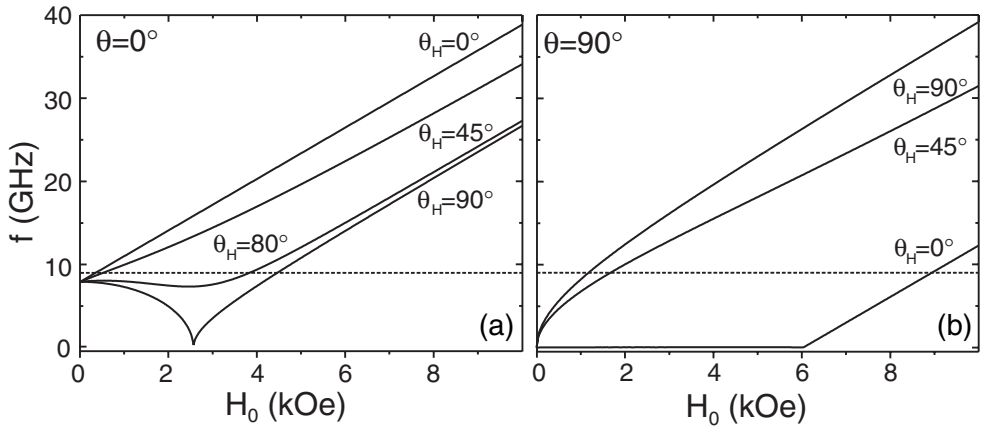

Figure 3. Resonance frequency as a function of the external field for a film having an easy axis out of plane (a) and an easy axis in plane (b) for several orientations of the external magnetic field θ_H.

left-hand panel of figure 3 it was therefore necessary to include a K_2-term with positive sign, $K_2 = 14.3\ \mu$eV/atom. The FMR measurements are made at fixed frequency, so that the points where the microwave level (dashed line for $f = 9$ GHz) crosses the calculated curves give the resonance positions for this particular frequency. For $\theta = 90°$ (right-hand panel) and for all angles of the external field only one H_{res} is possible. While rotating the external field out of the film plane the position of the resonance moves to larger fields, indicating the easy in-plane character of the system. For an easy axis out of plane ($\theta = 0°$, see left-hand panel) the occurrence of two energy minima as mentioned above leads to two resonances when the external field points along the hard axis ($\theta_H = 90°$). One appears at small fields and another at higher field values where the magnetization and external field are aligned parallel. Upon rotating the field out of the film plane closer to the easy axis by only some degrees, the resonances vanish. This leads to the situation where along the easy direction no signal can be observed and only within a small region around the hard axis are two signals detected. Therefore, it is impossible to measure the complete angular dependence. To avoid this, i.e. also to have the full angular dependence for the films having an easy axis out of plane, there are two methods.

(i) The frequency of the microwaves is increased which means upshifting the dashed line in figure 3. This is not possible within our *in situ* set-up.
(ii) In figure 3 the crossing point of the left-hand branch of the curve for $\theta = 90°$ with the y-axis is given by the out-of-plane anisotropy of the film.

For smaller anisotropy values this point can be brought below the microwave level, so that the whole angular dependence is detectable. Since for ultrathin films the anisotropy is a function of film thickness [2], this is equivalent to choosing the right film thicknesses.

Now we come to the mode intensities; the linewidth will be discussed separately in section 6.2. When the coupling is zero ($J_{inter} = 0$) the intensity I of the microwave absorption for each magnetic layer has to be found separately. For the external field $\vec{H}_0$ being either in or out of plane it is possible to give analytical expressions for I. For these two directions the coordinate systems introduced in section 3.2 coincide. The only difference is that for the in-plane direction the $-y'$-direction has to be transformed into the z-direction by multiplying

by -1. In the following discussion we therefore consider the $x/y/z$-system. For the in-plane configuration ($\vec{H}_0 \| y$, $\vec{h}_{rf} \| x$, the precession orbit of the magnetizations will be elliptical and lie in the x/z-plane. For this case and for a fixed value of the microwave power I for layer i is given by

$$I_{\|,i} \propto \frac{\left(\int_0^{d_i} m_{x,i}\,\mathrm{d}z\right)^2}{\frac{1}{2M_{S,i}}\int_0^{d_i}(m_{x,i}^2 + m_{z,i}^2)\,\mathrm{d}z}. \tag{31}$$

By assuming that $m_{x,i}$ and $m_{z,i}$ are uniform across the film i, one can solve the integral in equation (31)

$$I_{\|,i} \propto \frac{2(d_i m_{x,i})^2}{\frac{d_i}{M_{S,i}}(m_{x,i}^2 + m_{z,i}^2)} = 2M_{S,i}d_i\frac{m_{x,i}^2}{m_{x,i}^2 + m_{z,i}^2} = \frac{2M_{S,i}d_i}{1 + (H_{res,i}\gamma_i/\omega)^2}. \tag{32}$$

The quantity $m_{x,i}^2/(m_{x,i}^2 + m_{z,i}^2)$ is called the ellipticity factor. Using the explicit expressions for $m_{x,i}$ and $m_{z,i}$ as given by equation (25) and the resonance condition (equation (29)) for the in-plane direction, the ellipticity factor takes the form as given by the last expression of equation (32).

For the case where the external field is applied along the film normal, the magnetizations precess in the x/y-plane. Now the precession will take place in a circular orbit, since there is rotational symmetry around the film normal. In this case one takes for the time-dependent component of the magnetizations along the microwave direction $m_{x,i}$ while $m_{z,i} = 0$, so that equation (31) reduces to

$$I_{\perp,i} \propto \frac{\left(\int_0^{d_i} m_{x,i}\,\mathrm{d}z\right)^2}{\frac{1}{M_{S,i}}\int_0^{d_i} m_{x,i}^2\,\mathrm{d}z}. \tag{33}$$

Assuming again that $m_{x,i}$ is uniform over each film, equation (33) yields

$$I_{\perp,i} \propto \frac{(d_i m_{x,i})^2}{\frac{d_i}{M_{S,i}}m_{x,i}^2} = M_{S,i}d_i. \tag{34}$$

For this case the ellipticity factor is unity. Because of equations (32) and (34) for both the in-plane and out-of-plane geometry, the intensity of the resonance from a single film is proportional to the saturation magnetization $M_{S,i}$ times the film thickness. In addition, I is proportional to the ellipticity factor which is given by the time dependent magnetization components. The form of the ellipticity factor shows that in order to observe a FMR mode, the system must have a net rf magnetization component along the pumping field direction (in our case the x-direction). The precessional motion for one single film is illustrated in figure 4 for both geometries. For the parallel situation the ellipticity factor depends on the resonance frequency and thus on the resonance field. For the out-of-plane geometry, for which the ellipticity factor is constant, the intensity is independent of the two.

3.4. Trilayer and multilayer

This section discusses the case of N coupled layers (equation (21)) and focuses on the special case $N = 2$ of the trilayer described by equation (26). Most of the results can be easily extended to more magnetic layers.

3.4.1. Resonance fields. According to the number of solutions of equation (21) for N magnetic layers there are N modes supported by the layered structure, because there is one degree of freedom for each layer. There is one $q_\perp = 0$ mode, called the acoustical mode,

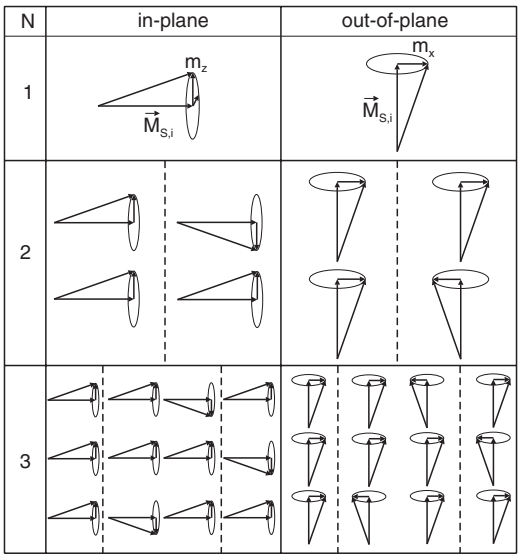

Figure 4. Schematic picture of the coupled uniform precession modes for films with $N = 1$–3 magnetic layers. Easy axis and $\vec{H}_0$ in plane (left) and out of plane (right), respectively.

where all the N magnetizations precess in phase, and $N - 1$ optical modes. With increasing mode number there will be more magnetizations which precess out of phase until for the optical mode with highest mode number the magnetizations in *adjacent* films precess out of phase. For the special case of the trilayer ($N = 2$) the picture predicts two modes, an acoustical and an optical one. For the latter the two magnetizations rotate out of phase, for the other one in phase. In the following the positions of the modes are discussed. Figure 5 shows the solution of equation (26). In the upper two panels the microwave frequency as a function of H_0 for ferromagnetic coupling is shown. In the literature such diagrams are often called dispersion relations and should not be confused with plots of the frequency as a function of the wavevector. They illustrate the results from equation (26). In (a) the behaviour for the external field applied in the film plane is shown, whereas in (b) the out-of-plane geometry is plotted. The frequency of $f = 9$ GHz used in most of our experiments is plotted as a dashed line. The intersections of this line with the acoustical (solid line) and optical (dotted line) mode branches define the resonance fields H_{res} for the two modes. In the lower two panels the equilibrium angles $\theta^0_{1,2}$ and $\varphi^0_{1,2}$ of the two magnetization vectors are displayed as a function of H_0 for the same trilayers as shown in (a) and (b). For simplicity two identical films with $2K_{2,i}/M_i = 0$, i.e. no intrinsic anisotropy, have been assumed in figure 5. The only term which produces anisotropy is $4\pi M_i$, i.e. the shape anisotropy. For the calculation and for both films $M_1 = M_2 = 0.485$ kG, the magnetization of bulk Ni at room temperature, has been assumed and a value of $J_{inter} = 10.9\ \mu$eV/atom is used for the ferromagnetic coupling. For $\theta_H = 90°$ (figure 5(a)) there are two branches. The optical branch is upshifted in frequency, which implies that one needs higher energy to excite it. This is because in the optical mode the two magnetizations are canted to each other, i.e. they deviate from the energy minimum favouring a parallel alignment for all values of H_0 as can be seen in figure 5(c). Therefore, the optical mode appears at higher frequencies or, for a constant frequency, at lower resonance fields. The mode separation is given by $H_{ex} = 2J_{inter}[1/(M_1d_1 + M_2d_2)]$. In general the separation is also influenced by the anisotropies of the two films (see section 5.2.1). When the

external field is rotated out of the film plane (figure 5(b)) these results are still valid at field values *larger* than the shape anisotropy. A complication arises for small external fields where $\vec{H}_0$ and $\vec{M}_1$, $\vec{M}_2$ are not parallel due to the anisotropy favouring an in-plane alignment. As the field increases the two magnetizations gradually rotate out of the film plane (figure 5(d)). Because of the ferromagnetic coupling both magnetizations stay parallel during this rotation. In the dispersion relation figure 5(b) the rotation leads to the behaviour at low field values. With increasing field the optical mode has lower frequency, whereas the acoustical mode stays at zero frequency until the system reaches the parallel state. Figure 6 shows the dispersion relation for the same system as discussed in figure 5. This time, however, an antiferromagnetic coupling of $J_{inter} = -4.5\ \mu$eV/atom was assumed. For antiferromagnetically coupled films there always exists a region where both magnetizations are antiparallel and therefore not parallel to the applied field. For H_0 along the film plane ($\theta_H = 90°$) and starting from zero field the two magnetizations are oriented antiparallel within the film plane. Due to the fact that both films were assumed to have an easy in-plane character, the two magnetizations rotate within the film plane as the field is increased. This is clearly shown in figure 6(c), where $\varphi^0_{1,2}$ gradually approach each other until the two magnetizations become aligned parallel. In order to achieve a parallel alignment for the out-of-plane direction the external field has to surpass the shape anisotropy which tries to keep the $\vec{M}_i$ in the film plane. Once the magnetizations are parallel the dispersion of figures 6(a) and (b) presents a similar behaviour as found for ferromagnetic coupling. Again the coupling can be determined from the mode separation given again by H_{ex}. Compared to the ferromagnetic coupling the mode positions of optical and acoustical modes are reversed with respect to the ferromagnetic case. Now the optical mode appears at lower frequencies or higher resonance fields because the canted configuration has lower energy than the parallel alignment within the acoustical mode. Thus, the relative positions of optical and acoustical mode can be used to identify the sign of J_{inter}. Furthermore, the exact mode positions reflect the absolute value of J_{inter} when they are analysed in the context of equation (26) described in section 3.2.

Within an FMR experiment the frequency is fixed, so that one always operates at a constant line parallel to the field axis in the dispersion relation (the 9 GHz line in figures 5 and 6 is one example). Figure 7 schematically shows FMR spectra for trilayers at a fixed frequency of 9 GHz for the case where $\vec{H}_0$ is applied in the film plane. It is assumed that the frequency is large enough that one only probes the region where both magnetizations are aligned parallel to $\vec{H}_0$. The solid curves indicate the signals of two slightly different magnetic films which do not interact. This is the situation for two films separated by an infinitely large spacer layer, where both films have their individual resonance fields. When the spacer thickness is reduced, the two films become coupled. As shown by the dashed lines, the coupled system presents two eigenmodes, the acoustical and optical mode, which are formed by the uniform modes of the individual films. It is important to note that the coupled modes do not belong to one film only. They merely arise from both magnetic layers. Both move towards higher (lower) field values within the coupled system for ferromagnetic (antiferromagnetic) coupling. In addition, the intensity of the optical mode decreases, whereas more oscillator strength is coupled into the acoustical one so that its intensity increases. For stronger coupling, i.e. larger values of J_{inter} (dotted curves), both modes are even more shifted relative to the resonance fields in the uncoupled system and the intensity ratio between optical and acoustical modes is further decreased.

When only discussing the regime where the $\vec{M}_i$ are parallel to the field, the extension of the picture to more magnetic layers is straightforward, whereas for the non-parallel regime one has to calculate the mode spectrum to analyse the data and to identify the modes and their positions. Figure 4 illustrates the possible modes of the coupled system in the parallel regime for N ranging from 1 to 3 and for external fields either in the film plane or normal to the film

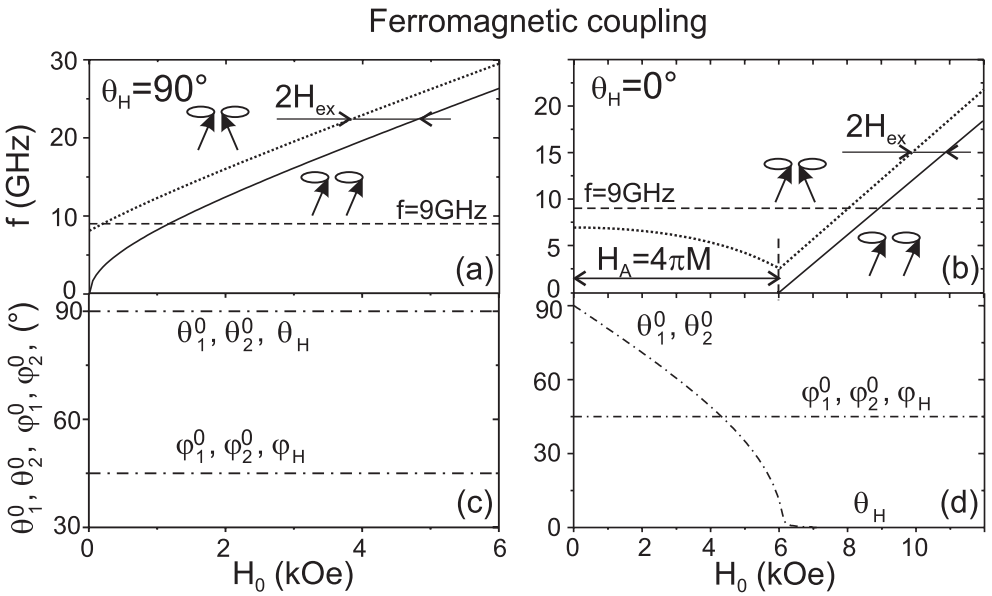

Figure 5. Dispersion relation for a ferromagnetically coupled trilayer for $\vec{H}_0$ in plane ((a), (c)) and out of plane ((b), (d)). The solid (dotted) line in ((a), (b)) corresponds to the acoustical (optical) mode. In ((c), (d)) the in-plane ((φ^0) and out-of-plane (θ^0) equilibrium angles for the two magnetizations as a function of H_0 are shown. φ_H and θ_H denote the direction of the external field.

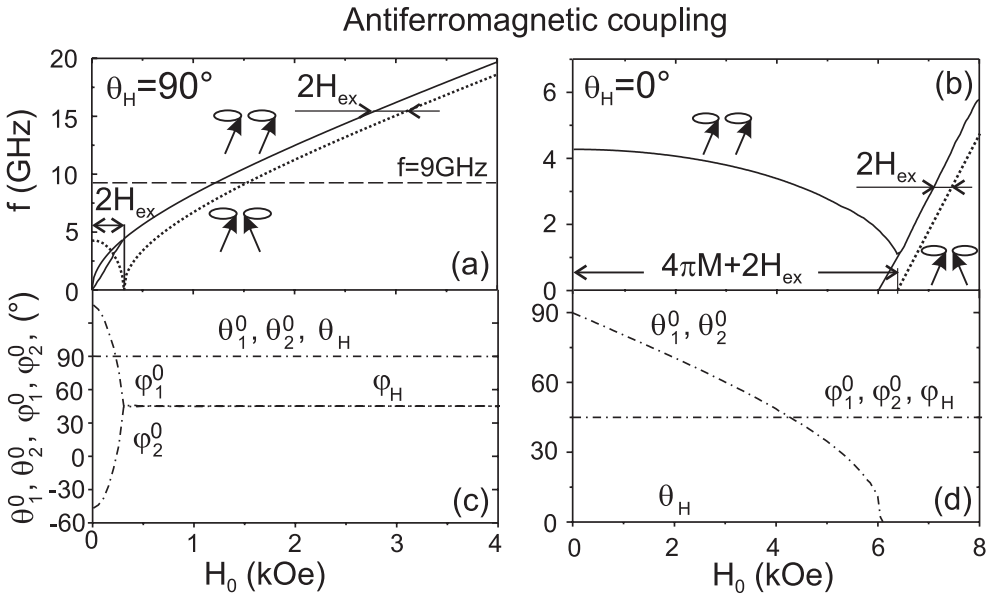

Figure 6. Dispersion relation for an antiferromagnetically coupled trilayer. The notation is the same as in figure 5.

plane. The vectors correspond to the uniform modes within a film, which become coupled together in the multilayer. For $N = 2$ only one acoustical and one optical mode are possible as has just been discussed. For $N = 3$ one has more possible modes. The acoustical mode where

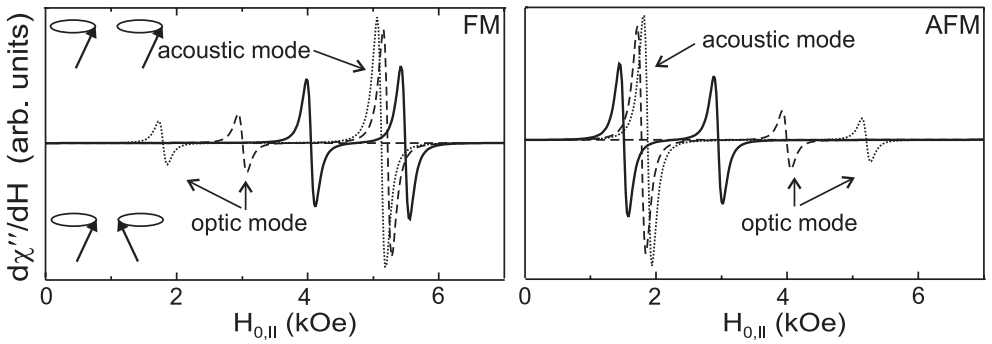

Figure 7. Simulation of the FMR spectrum for a ferromagnetically (left-hand panel) and antiferromagnetically (right-hand panel) coupled trilayer. The solid spectra show the FMR signal for the two films without coupling and the dashed and dotted spectra show the signal after introducing a coupling with increasing strength.

all three magnetizations precess in phase is the lowest energy state for ferromagnetic coupling. For antiferromagnetic coupling it is the highest one. The opposite behaviour shows the optical mode where all neighbouring $\vec{M}_i$ precess out of phase (right-hand plot in the lowest panel). There are more possibilities realized by the two mode profiles in the middle. For these modes which are degenerate in energy only one magnetization rotates out of phase, so that the energy of the modes lies in between the two extreme cases. For $N = 3$ one therefore expects to have three resonances and the acoustical one again is on the higher field side of the two optical ones for ferromagnetic coupling and on the lower field side for antiferromagnetic coupling. Again the position of the acoustical mode in the regime where $\vec{H}_0$ and the $\vec{M}_i$ are parallel is a well defined criterion for the sign and value of the coupling.

3.4.2. Mode intensities. If the N films are coupled, equations (32) and (34) still describe the intensities of the N modes provided the time dependent magnetizations $\vec{m}_i(t)$ for each of the modes are known. Then, for a given value of J_{inter}, one can calculate the intensity I for each mode by summing up the quantities given in equations (32) and (34) over the N layers. For the in-plane configuration one has

$$I_{\parallel} \propto \frac{2\left(\sum_i^N d_i m_{x,i}\right)^2}{\sum_i^N \frac{d_i}{M_{S,i}}(m_{x,i}^2 + m_{z,i}^2)}. \tag{35}$$

For the out-of-plane geometry one gets

$$I_{\perp} \propto \frac{\left(\sum_i^N d_i m_{x,i}\right)^2}{\sum_i^N \frac{d_i}{M_{S,i}} m_{x,i}^2}. \tag{36}$$

Figure 4 can also be used to explain how the intensities of the modes will change from their value for the non-coupled case given by the equations (32) and (34) upon increasing the value of J_{inter}. While the relative position of the acoustical and optical modes depends on the sign and the value of the coupling, the relative mode intensities only depend on the absolute value. The following discussion is therefore valid for ferromagnetic as well as for antiferromagnetic coupling of the films. According to equations (35) and (36) the *sum* of the time dependent magnetizations determines the intensity for a resonance mode within the coupled films. Figure 4 shows the case $N = 2$, i.e. for the trilayer for in- and out-of-plane geometry. When the magnetization vectors are saturated, the in-phase (acoustical) mode leads to a large microwave absorption, since both rf magnetizations are always aligned parallel and add up. For the optical mode, however, the

two $\vec{m}_i$ have opposite sign and subsequently the intensity will be relatively small. When the two films are identical, i.e. when they have the same effective magnetization M_{eff}, the intensity of the optical mode will be zero. In detail the intensity of the optical mode is proportional to the difference in effective magnetization of the two films and inversely proportional to J_{inter}, i.e. to the quantity $|M_{eff,1} - M_{eff,2}|/J_{inter}$. This will be discussed in section 5.2. For three coupled films ($N = 3$) it is not possible that all rf magnetizations cancel to zero. Therefore, one expects one acoustical mode and two optical ones, even for three identical films. Again the largest intensity is coupled into the acoustical mode, whereas the optical modes have smaller intensity (see figure 4). For a larger number of films the picture is extended accordingly. For N identical films all modes have non-zero intensity in the case where N is an odd number, whereas for N an even number some modes will vanish. If the films are different, all modes can have a non-zero intensity.

4. Experimental details

Before comparing our experimental results with the theoretical predictions, the systems used to study the interlayer coupling are introduced. The FMR measurements were performed partially at 4 GHz, but most experiments were done at 9 GHz. Details concerning the FMR apparatus are given in [2, 4]. Since prototype systems are needed it is particularly important to investigate in a first step the structural properties of the systems before performing the magnetic measurements. The film preparation and FMR measurements were performed in a UHV system with a base pressure of 5×10^{-11} mbar. All trilayer systems were grown on Cu(001) single-crystal substrates which have been cleaned by cyclic Ar-ion etching and annealing to 830 K until the surface showed sharp low-energy electron-diffraction (LEED) patterns and no detectable contamination in the Auger electron spectra could be observed. Details of the substrate preparation are reported in [28]. Most studies on coupled 3d metals deposited on Cu(001) are done for Fe and Co, whereas less work has been done for Ni. In contrast to Ni and Co the growth of Fe on Cu(001) is structurally problematic [29]. Therefore, we focus our investigations on Ni based trilayers having either two Ni layers or one substituted by Co. In addition, we compare the results to trilayers consisting of two Co layers. The pressure during film preparation could be kept below 2×10^{-10} mbar in the case of Co and Ni and 3×10^{-10} mbar in the case of Cu. The growth of the 3d metals Co and Ni on Cu(001) is well understood and allows us to produce epitaxially grown films of high quality [29]. For both cases stable face-centred cubic (fcc) structures with a tetragonal distortion, often referred to as face-centred tetragonal (fct), are formed. The interatomic distance for bulk Cu is 2.56 Å whereas the values for Ni and Co are 2.49 and 2.505 Å, respectively. This leads to an in-plane lattice mismatch of 2.5% for the Ni/Cu(001)- and 2.0% for the Co/Cu(001) system and results in a pseudomorphic growth up to more than 15 ML for both systems [30]. The growth conditions like the deposition rate or the deposition temperature strongly influence the growth behaviour. A slight increase of the deposition temperature can lead to a better layer-by-layer growth but also increases the rate of interdiffusion between the film and the substrate. On the other hand low deposition temperatures decrease the probability of intermixing, but usually lead to three-dimensional growth due to the limited diffusion of the adatoms on the surface. For the deposition of Ni and Co films around room temperature the intermixed area was shown to be restricted almost to only the first ML and good layer-by-layer growth was achieved [30–33].

4.1. The Cu/Ni/Cu/Ni/Cu(001) system

During the evaporation of the trilayer structures the intensity of the specular medium-energy electron-diffraction (MEED) spot is recorded, so that the growth can be monitored on line. As

an example the MEED intensity during the preparation of a Cu/Ni/Cu/Ni/Cu(001) trilayer is presented in the left-hand panel of figure 8. The lowest curve shows the MEED intensity during the deposition of 10 ML Ni at room temperature. The intensity oscillates, indicating a good layer-by-layer growth during the deposition of the first Ni layers, while the oscillations almost vanish before all ten layers are evaporated. This growth of Ni on Cu(001) at room temperature is well known and may be explained with a transition towards a three-dimensional growth mode at around 5 ML where the Ni film starts to form quadratic pyramids. In figure 9(a) an STM picture taken at room temperature of a 9 ML thick Ni film is shown, where one clearly sees the pyramids having their edges along the ⟨110⟩-directions. After annealing the Ni film for 10 min at $T = 420$ K the pyramids are removed as shown in figure 9(b) for the same film as shown in (a). In order to have a better control of the Ni film thickness, we slightly increased the deposition temperature to values of $T = 330$ K *during* the growth. The result is shown by the upper curve in the left-hand panel of figure 8 where 9 ML Ni are evaporated at $T = 330$ K. Comparing the MEED intensity with the one for room temperature deposition (lowest curve) one sees that the oscillations slightly improve at higher temperatures, leading to an extension of the oscillatory behaviour towards large film thicknesses. This indicates that the growth is less rough, which in turn reduces the error in the thickness determination to ± 0.1 ML. The next step is to deposit the Cu spacer which is also shown in figure 8. One can hardly see two MEED oscillations. This finding is supported by STM pictures shown in figure 9(c), where 5 ML Cu on top of a Ni film are presented. A clear tendency towards three-dimensional growth is seen, explaining the MEED result. For Cu it was not possible to improve the MEED oscillations on top of Ni films even after increasing the substrate temperature. Therefore, the deposition rate for Cu was taken from MEED oscillations found for Cu on Co/Cu(001) films (see below) which leads to a larger uncertainty in the Cu thickness of ± 0.2 ML for the Cu/Ni/Cu/Ni/Cu(001) trilayers compared to the Ni/Cu/Co/Cu(001) systems. Prior to the deposition of the topmost Ni film the Cu spacer was smoothened by annealing for 10 min at $T = 420$ K. The surface after this process for the same Cu spacer as shown in figure 9(c) is presented in figure 9(d). All islands are removed and the surface cannot be distinguished from the one of the Cu(001) substrate. Auger spectra taken before and after the annealing did not show any difference, i.e. no interdiffusion was observed. In a last step the second Ni film is deposited on top of the Cu spacer as shown in figure 8 for a Ni film of 8 ML. It should be noted that because of its three-dimensional growth at room temperature the Cu/Ni/Cu/Ni/Cu(001) system is also best suited for the investigation of the influence of rough interfaces on the coupling between the two magnetic layers which will be discussed in section 6.1. Finally, the topmost Cu cap layer is deposited (not shown in figure 8) to ensure that the two Ni films both have Curie temperatures close to each other, since capping layers usually reduce T_C [34]. In addition, the effect of a non-magnetic overlayer on the value of J_{inter} can be studied (see section 6.1).

4.2. The Ni/Cu/Co/Cu(001) system

The right-hand panel of figure 8 shows the deposition of a Ni/Cu/Co/Cu(001) trilayer which again is controlled via MEED oscillations. The upper curve shows the deposition of 2 ML Co onto the Cu(001) substrate leading to well defined MEED oscillations. In a next step 5 ML Cu are evaporated on top of the Co film. Again the MEED intensity shows clear oscillations. However, the amplitude is damped, indicating that the film starts to become three dimensional. To smoothen the Cu spacer before the deposition of the topmost Ni film the spacer was therefore annealed for 10 min at $T = 420$ K as in the case of the Cu/Ni/Cu/Ni trilayers. Auger spectra taken before and after the annealing process showed no indication of intermixing between Co and Cu due to the annealing. This is in accordance with experiments for Co/Cu(001) where

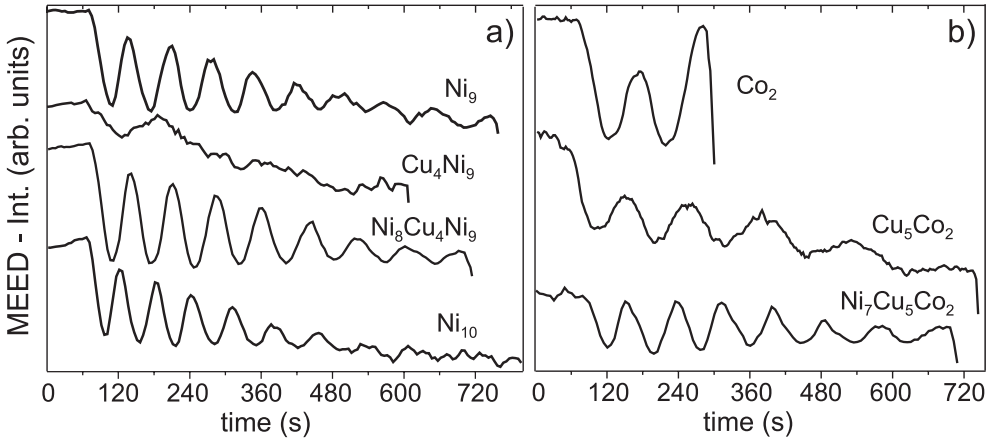

Figure 8. MEED oscillations for (left-hand panel) the Cu/Ni/Cu/Ni/Cu(001) system and (right-hand panel) the Ni/Cu/Co/Cu(001) system. The number of MLs is given as a subscript.

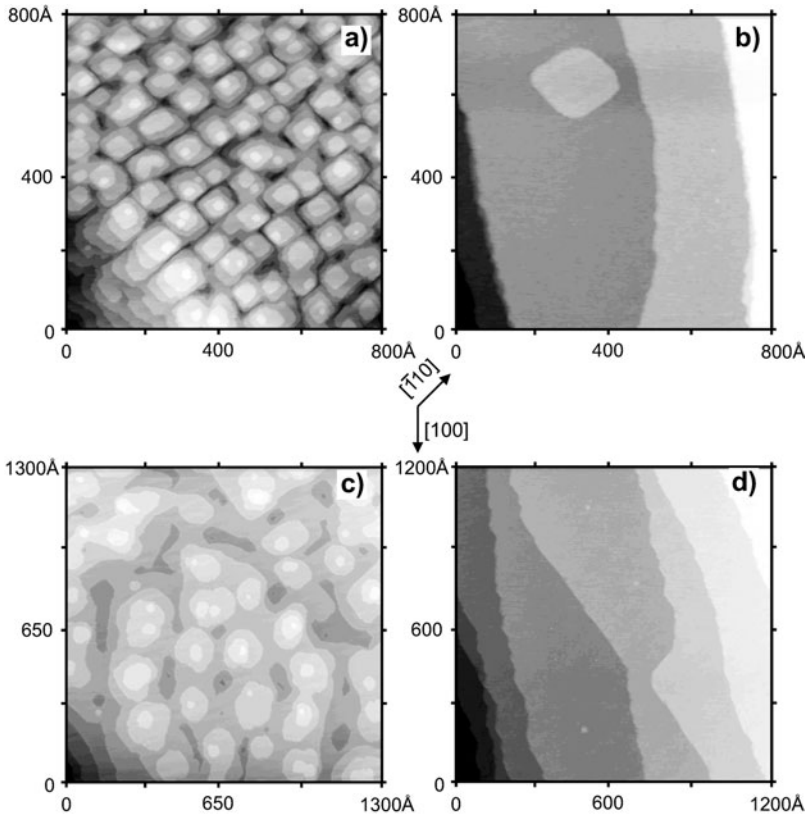

Figure 9. STM images taken after successively depositing (a) 9 ML Ni and (c) 5 ML Cu on Cu(001). (b) and (d) show the surface after a 10 min annealing to $T = 420$ K of the films shown in (a) and (c), respectively.

the maximum safe annealing temperature is shown to be about 450 K. Finally, 7 ML of Ni are deposited on top of the Cu spacer (see the lowest curve in figure 8) in the same way as described for the Cu/Ni/Cu/Ni/Cu(001) trilayer.

5. Comparison of experiment and calculation

5.1. In situ FMR in single-film systems

Before the trilayers themselves are investigated, it is useful to characterize the single-film systems. Therefore, we have measured our films

(i) after deposition of the bottom magnetic layer and
(ii) after evaporation of the Cu spacer on top of it.

We performed temperature and angular dependent measurements. By using equation (28) the effective field M_{eff} and the anisotropies can be determined from the experiment. A detailed description of this procedure is given elsewhere [35, 36]. The angular dependent measurements were made by changing the polar angle θ_H (see figure 2) of the sample. In the following the single films are discussed with regard to the trilayers. A complete FMR study of single films grown on Cu(001) may be found in [2] for Ni and in [18] for Co.

5.1.1. Co films. Ultrathin Co films on Cu(001) show a jump in T_C at about 1.8 ML [37] caused by bilayer island growth within the second ML [38]. Such thin layers are therefore not well suited for well defined trilayers. On the other hand the T_C of Co films thicker than 2 ML increases rapidly. To have the possibility of measuring up to T_C without the problem of intermixing, we have chosen Co films with a thickness of 2 ML which have a T_C below 400 K. In figure 10 the full out-of-plane angular dependence for 2 ML Co (a) and for the same film after capping with 3 ML of Cu (b) measured at room temperature is shown. The insets show FMR spectra for the indicated θ_H-values. For both cases and for all angles of the external magnetic field only one resonance signal is found which is in agreement with the case of a film having an in-plane easy axis of magnetization as discussed in figure 3(a). A fit according to equation (28) (solid curve) is plotted together with the data. The fit yields the effective magnetization $M_{eff} = -42$ kG for the bare Co film and $M_{eff} = -38$ kG after capping. The negative value again indicates that the film exhibits an easy axis within the film plane ($\theta = 90°$). The smaller value of M_{eff} after capping is mostly due to a reduction of T_C leading to a reduction of the film magnetization. To precisely determine the in-plane anisotropy given by the constant $K_{4\parallel}$ one would in principle need an in-plane angular dependent measurement. However, the shape of the out-of-plane angular dependence is also influenced by $K_{4\parallel}$ [2] and can therefore be used to estimate the value of the in-plane term. The fits displayed in figure 10 are performed with $K_{4\parallel}/M = -0.03$ kG in the case of the bare Co film and $K_{4\parallel}/M = -0.06$ kG for the Cu capped system. Fits using no in-plane anisotropy ($K_{4\parallel}/M = 0$ kG) included in figure 10 (dashed curves) agree less with the data. A negative $K_{4\parallel}$ for the Co film indicates an in-plane easy axis along the [110]-direction which is well known for this system. The values of $K_{4\parallel}$ are much smaller than the out-of-plane anisotropy given by M_{eff}, and thus the resonance field of the Co film is mostly determined by the latter.

5.1.2. Ni films. A similar behaviour to the one just described for Co is found for Ni films on Cu(001) with thicknesses below 10–11 ML, where the film magnetization for Ni lies in the film plane. For larger thicknesses Ni films show a spin reorientation transition (change in sign of M_{eff}) which drives the magnetization out of the film plane [2]. This transition is shifted

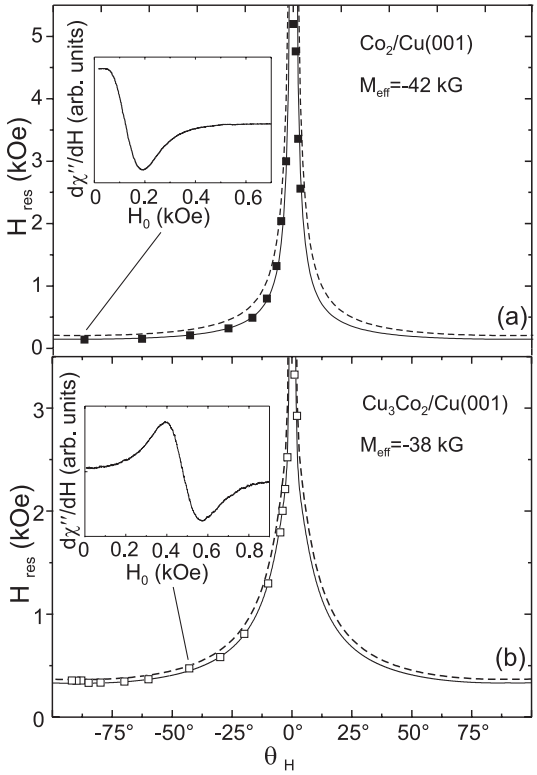

Figure 10. Angular dependence for 2 ML Co on Cu(001) (a) without and (b) with Cu cap layer. The dashed curves are fits neglecting the in-plane anisotropy term $K_{4\|}$.

down to about 7.5 ML when capping the films with Cu [39]. In addition, the T_C is reduced by a Cu overlayer. The complete out-of-plane angular dependent measurement for Ni at room temperature is shown in figure 11, where H_{res} as a function of θ_H for 8 ML of Ni/Cu(001) (a) and 9 ML of Ni/Cu(001) (b) is plotted. In each panel we show the results before (filled circles) and after capping the film with 4 ML of Cu (open circles). For the bare Ni films the negative values of M_{eff} indicate an easy axis in plane. The smaller value of the Ni_9 film[3] shows that this film is closer to the spin reorientation at about 10–11 ML, where M_{eff} is close to zero, and thus the higher order anisotropy constants become important [2]. After capping the two films with Cu the minimum of H_{res} moves from $\theta_H = 90°$ to 0°. This means that the easy axis has switched from in the film plane towards the film normal. This change of the easy axis is also reflected in the positive sign of M_{eff}. Besides the sign of M_{eff} its value is larger for the Cu_4Ni_9 film compared to the Cu_4Ni_8 film which means an increase of the out-of-plane anisotropy within the Cu capped Ni films. This trend is continued with increasing Ni thickness (figure 12).

Figure 12(b) shows the dispersion curves according to equation (28) as determined from experimentally measured H_{res}-values for Ni films with thicknesses ranging between 8 and 12 ML already capped with Cu. The external field was aligned along the in-plane direction ($\theta_H = 90°$). Thus, the crossing points of the 9 GHz line indicate the resonance fields. Figure 12(a) shows the original FMR spectra for the smallest 8 ML and the largest 12 ML Ni

[3] Here and in the following the number of MLs is given as a subscript.

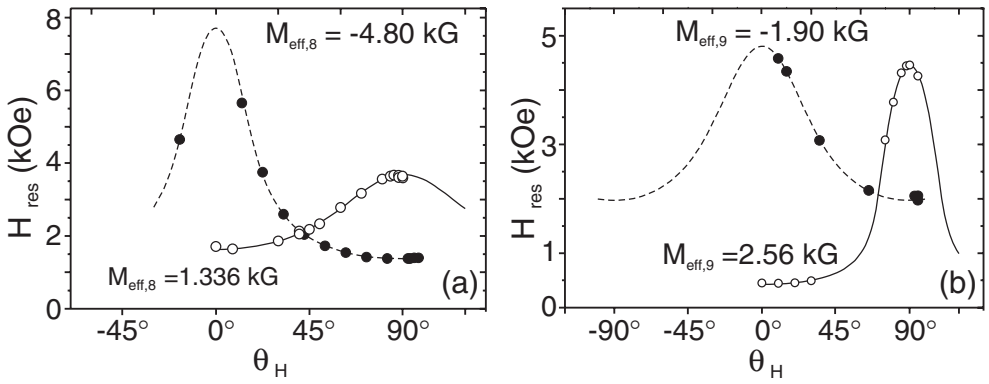

Figure 11. Angular dependence for (a) 8 and (b) 9 ML Ni on Cu(001) with (solid curve) and without (dashed curve) Cu cap layer.

thickness. For 12 ML two resonances are observed. This behaviour can be explained with an increase in the perpendicular anisotropy and corresponds to the case of a film having an out-of-plane easy axis of magnetization as discussed in figure 3(b). The complete analysis presented in figure 12(b) indicates that the positive values of M_{eff} increase with Ni thickness. Therefore, two resonances are observed for thicknesses larger than 10 ML. The transition between observing one and two signals is observed for the 10 ML film. In figure 13 this film was measured at different temperatures in the range 300–400 K. One sees in (b) that due to the decrease of M_{eff} at higher temperatures the left-hand branch of the dispersion curve moves below the 9 GHz line, so that only one signal is observed at larger T-values. The transition between observing one and two signals can be seen more directly in figure 13(a), where the measured resonance fields of the film are plotted as a function of the temperature. At room temperature one observes two signals which are also shown in the inset for $T = 313$ K. The resonance field for the signal at low field values moves towards smaller fields until it vanishes at about $T = 375$ K. Above 375 K only one resonance is observed as shown in the inset for $T = 380$ K which stays even up to the highest temperature of 400 K. The occurrence of more than one resonance signal in the single films complicates the analysis in the trilayers. To avoid such problems, the Ni thicknesses were chosen to be 8–9 ML within the trilayers with out-of-plane magnetized films.

5.2. In situ FMR in trilayer systems

5.2.1. Determination of J_{inter}. In section 3.4 it was shown how the coupling constant J_{inter} can in principle be determined from FMR experiments. However, one has to note the following: the analysis is usually complicated because the positions of the modes are not only determined by the coupling alone, but are rather a function of J_{inter} and the anisotropies of the individual layers. In this case the problem arises that when only a measure of the *coupled* system is possible it is not easy to extract all anisotropy values from angular dependent measurements. We therefore used a new approach which works when the films are subsequently deposited and measured in a UHV system. After the preparation of the first magnetic layer its anisotropy can be determined. Then, the next layer is deposited and the whole system is measured. Now the properties of the bottom layer are known so that only the ones of the topmost film have to be deduced. We will explain the procedure by using an example of a $Cu_4Ni_8Cu_5Ni_9/Cu(001)$ trilayer. In figure 14 the FMR spectra for this system measured at room temperature are

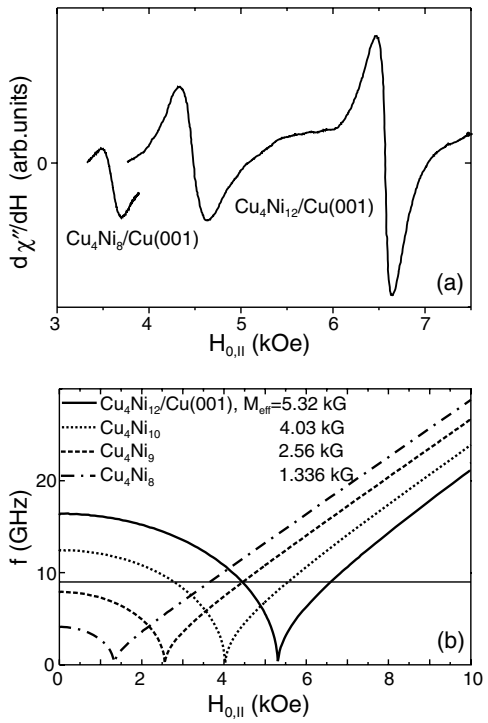

Figure 12. Cu capped Ni films with Ni thicknesses in the range 8–12 ML. (a) Measured resonance spectra for $d_{\mathrm{Ni}} = 8, 12$ ML. (b) Frequency as a function of the external field for $d_{\mathrm{Ni}} = 8, 9, 10, 12$ ML. The curves are calculated using the experimental values of the anisotropies. The intersection of the curves with the constant line for $f = 9$ GHz indicates the measured resonance fields.

shown. The dashed line indicates the *same* trilayer structure, before the deposition of the topmost Ni_8 film. The angular dependence measured for this single film has already been shown in figure 11(b). From this measurement the anisotropy of the bottom layer is obtained. In the trilayer one observes two resonances. The larger acoustical mode is located at higher fields with respect to the optical mode, and thus the system is coupled ferromagnetically. This is confirmed by the polar MOKE results from the same trilayer shown in the inset. One observes a rectangular loop showing that the two magnetizations flip together because of their ferromagnetic coupling. Apart from the sign of the coupling the Kerr effect does not allow us to deduce the value of J_{inter}. Within our *in situ* set-up the sign of the coupling may also be obtained from a direct comparison of the resonance field of the single bottom layer to the H_{res}-values of the modes in the trilayer. Compared to the single resonance of the bottom film the acoustical mode in the trilayer is shifted towards lower fields. This behaviour is exactly the one which was schematically shown in figure 7 and the shift is a measure of J_{inter}. To unambiguously extract J_{inter} from the field shift or from the two mode positions one needs in a last step to also deduce the anisotropy values for the *topmost* Ni film. Figure 15 shows how the anisotropy of the topmost Cu_4Ni_8 film is determined from the full angular dependence in the *coupled* system. Again the angular dependence for the bottom Cu_5Ni_9 film presented already in figure 11(b) is shown as a dashed curve. In figure 15 the experimental values of the optical (open squares) and acoustical mode (solid squares) are plotted together with a fit. The value of $M_{eff} = 1.136$ kG is smaller than the one found for the bottom film due to the

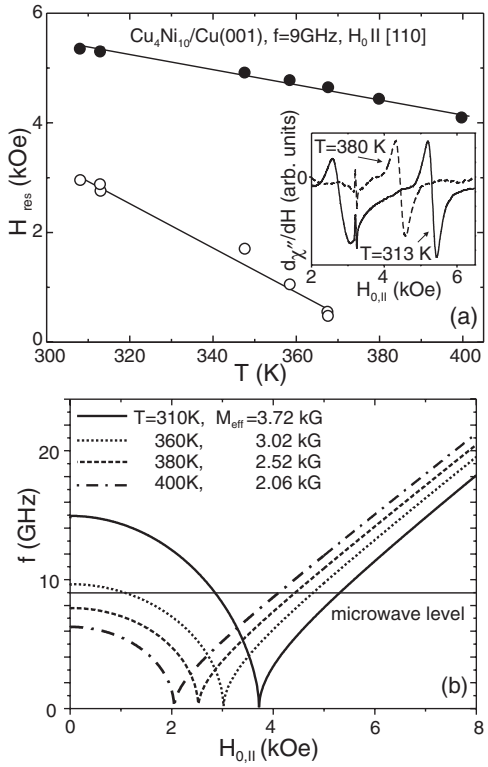

Figure 13. (a) Resonance fields as a function of the temperature for the two signals observed in a 10 ML thick Ni film capped by 4 ML of Cu. One of the signals vanishes at higher temperatures. The inset shows the spectra at two temperatures. (b) Microwave frequency as a function of the external field for various temperatures calculated for the same film as shown in (a). The calculation was performed such that the observed resonance fields are best reproduced by the intersections of the calculated curve with the 9 GHz line being the experimental frequency. From the calculation the anisotropy is derived despite the fact that not all of the angular dependence could be measured.

smaller thickness of the topmost layer. The positive value indicates that the topmost film also has an easy axis along the film normal. It is interesting to note that the angular dependence in coupled trilayers is in principle different from those known from single films. If the two films were uncoupled their different anisotropies would imply that one film has the larger H_{res} along the hard direction, but also the smaller H_{res} along the easy axis. This would then lead to a crossing of the two angular dependences at a particular angle. The dependences of optical and acoustical modes do not cross, i.e. for *all* θ_H-values the optical mode is located at lower H_{res}-values, reflecting the ferromagnetic coupling of the films. Taking the angular dependence of the bottom film only and the one measured in the coupled system, *all* unknown values influencing the H_{res} of optical and acoustical modes can be eliminated. Then, the only parameter left which determines the shift is J_{inter} itself. For the system shown in figure 14 J_{inter} equals 8.9 μeV/atom.

5.2.2. Resonance fields. A complete analysis of all resonance fields measured in $Cu_4Ni_8Cu_xNi_9/Cu(001)$ trilayers is presented in figure 16. The positions of the two modes for the external field in plane as a function of J_{inter} are displayed. Both magnetic layers are

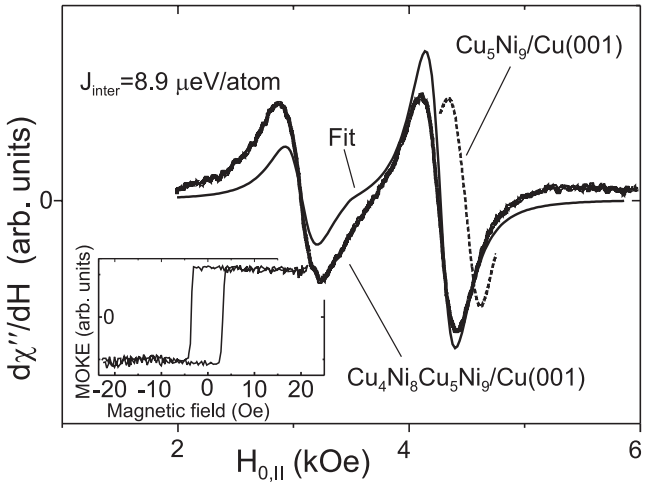

Figure 14. FMR spectrum measured for a $Cu_4Ni_8Cu_5Ni_9/Cu(001)$ trilayer (thick solid curve) together with the spectrum taken from the bottom $Cu_5Ni_9/Cu(001)$ film only (dashed curve). The thin solid line is a fit. Inset: hysteresis loop for the same trilayer obtained from polar Kerr effect.

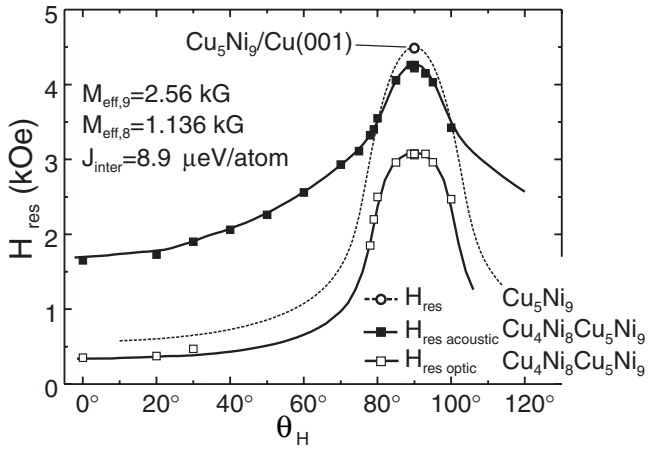

Figure 15. Angular dependence of the optical (open squares) and acoustical mode (filled squares) measured in the $Cu_4Ni_8Cu_5Ni_9/Cu(001)$ trilayer. The dashed curve shows the angular dependence for the bottom $Cu_5Ni_9/Cu(001)$ film only (figure 11(b)).

somewhat different and consequently they present different resonance fields for $J_{inter} = 0$. The black line corresponds to the theory for which the experimentally found anisotropy from the angular dependent measurements of the uncoupled Cu capped Ni_9 and Ni_8 film (see figure 11) was used. Upon increasing the strength of the coupling, one sees that for ferromagnetic coupling the acoustical mode approaches a fixed point, whereas the optical mode moves towards zero field. The trend is well reproduced by the data. For antiferromagnetic coupling (inset of figure 16) the acoustical mode is located at lower fields compared to the optical one, but again the acoustical mode approaches a fixed field value for large coupling. The optical mode now moves fast towards high fields. Independent of the sign of J_{inter} the coupled system behaves at large J_{inter}-values like a single film with an effective gyromagnetic ratio and an effective

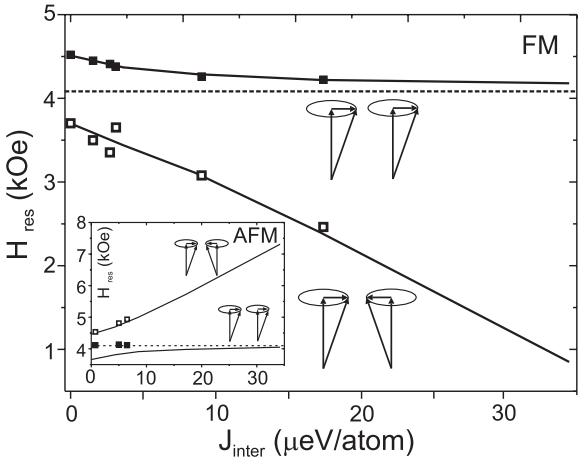

Figure 16. Mode position in a trilayer as a function of J_{inter} for ferromagnetic and antiferromagnetic (inset) coupling. The parameters used for the calculation are given in the text. The results from our measurements are plotted on top of the theory.

anisotropy field given by

$$M^*_{eff} = \frac{d_1 M_1 M_{eff,1} + d_2 M_2 M_{eff,2}}{d_1 M_1 + d_2 M_2}, \qquad \gamma^* = \frac{d_1 M_1 + d_2 M_2}{d_1 M_1/\gamma_1 + d_2 M_2/\gamma_2}. \quad (37)$$

The dashed lines in figure 16 show the fixed field value according to equation (37). Equation (37) can, for N magnetic layers, easily be extended if the numerator and denominator are replaced by a sum over all N layers.

5.2.3. Mode intensity. The behaviour of the intensities as a function of J_{inter} for different $Cu_4Ni_8Cu_xNi_9$/Cu(001) trilayers with $\vec{H}_0$ along the in-plane direction is plotted for the experimentally deduced anisotropy values in figure 17(a). The values have been normalized to the intensity of the signal from the Cu_xNi_9/Cu(001) film. The points indicate again our experimentally found intensities. Figure 17(a) shows that for increasing coupling strength more and more intensity is coupled into the acoustical mode, whereas the optical mode fades away. The intensity of the single mode which remains for strong coupling can be shown to be given for the in-plane geometry by

$$I_{\parallel} \propto \frac{2\sum_{i=1}^{N} M_{S,i} d_i}{1 + (H^{single}_{res,} \gamma^*/\omega)^2}. \quad (38)$$

Here γ^* is given by equation (37) and H^{single}_{res} is the resonance field at which, for strong coupling, the single resonance is observed. The dashed line in figure 17(a) indicates the intensity of the single resonance for strong coupling and was calculated via equation (38) with $N = 2$. Both optical and acoustical modes follow the theory in reasonable agreement. In particular, the acoustical mode approaches the dashed line for larger J_{inter}. For completeness we give the expression for the out-of-plane geometry. Here the intensity of the single line for strong coupling is simply the sum of the intensities of the individual layers.

$$I_{\perp} \propto \sum_{i=1}^{N} d_i M_{S,i}. \quad (39)$$

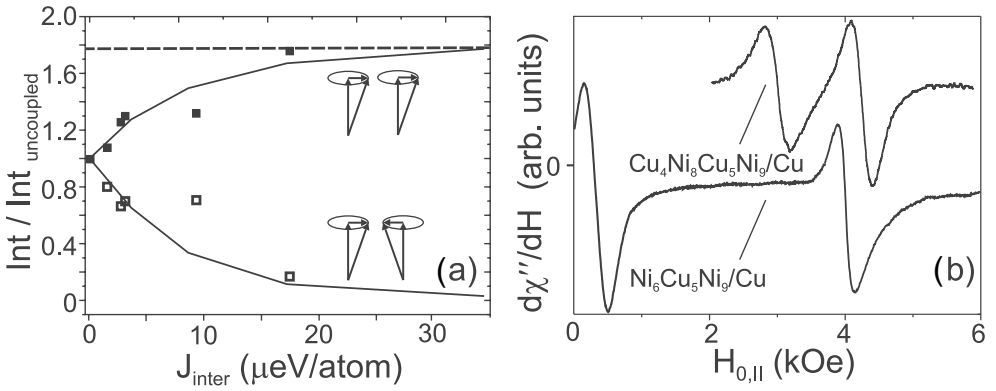

Figure 17. (a) Mode intensity as a function of J_{inter} for a trilayer. The parameters of the two films are the same as in figure 16. (b) FMR spectra for trilayers with the same value of J_{inter} but different values of M_{eff}.

Figure 17(a) shows that the optical mode intensity follows the $1/J_{inter}$ dependence as discussed in section 3.4. The other prediction was that the optical mode intensity should increase for larger values of $|M_{eff,1} - M_{eff,2}|$, i.e. when the anisotropies of the two coupled films are different. To show this effect, we plot in figure 17(b) two FMR spectra. The upper one which has been shifted upwards for better clarity results from the $Cu_4Ni_8Cu_5Ni_9/Cu(001)$ trilayer already shown in figure 14. The lower spectrum was taken from a $Ni_6Cu_5Ni_9/Cu(001)$ trilayer. Since 6 ML Ni on Cu(001) have an easy axis in plane [2], the anisotropy differs much from the one of the bottom $Cu_5Ni_9/Cu(001)$ film with easy axis out of plane as shown in figure 11. The anisotropy value of the $Ni_6/Cu(001)$ was deduced to be $M_{eff} = -4.2$ kG. The coupling for the $Ni_6Cu_5Ni_9/Cu(001)$ trilayer was found to be the same as the one for the $Cu_4Ni_8Cu_5Ni_9/Cu(001)$ trilayer. This comes from the fact that the spacer thickness is equal for the two trilayers. Figure 17(b) clearly shows that the optical mode intensity found in the $Ni_6Cu_5Ni_9/Cu(001)$ trilayer is much larger than in the $Cu_4Ni_8Cu_5Ni_9/Cu(001)$ trilayer due to the larger value of $|M_{eff,1} - M_{eff,2}|$, so that the optical mode has even more oscillator strength than the acoustical one. Moreover, the anisotropy does also influence the mode separation which is much bigger in the $Ni_6Cu_5Ni_9/Cu(001)$ trilayer.

6. Parameters that influence the coupling

To modify the coupling it is important to understand how it is influenced by specific parameters like the temperature or a protection layer. In this section we discuss such parameters. We do not aim to give a complete overview of each parameter. We rather focus on showing the advantages that *in situ* FMR provides. The discussion will be split into a part which investigates the influence on the resonance field and a second part which describes the influence on the linewidth.

6.1. Analysis of the resonance field

6.1.1. Influence of the spacer thickness. In the following the oscillatory behaviour of the interlayer exchange coupling given by J_{inter} is discussed. The values of J_{inter} were determined as described in section 5.2. Figure 18 shows J_{inter} as a function of the spacer thickness d_{Cu} for $Cu_4Ni_8Cu_xNi_9/Cu(001)$ (solid squares) as well as for $Ni_7Cu_xCo_2/Cu(001)$ trilayers (open

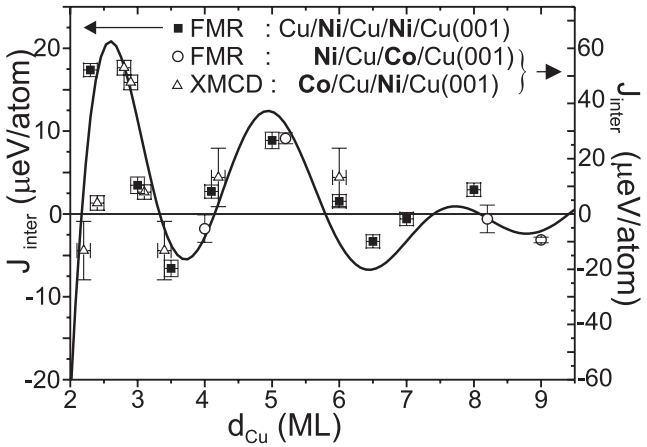

Figure 18. J_{inter} as a function of the spacer thickness d_{Cu} for all trilayer systems which were investigated.

triangles and open circles), i.e. the magnetic layer thickness and the overlayer thickness in the case of the $Cu_4Ni_8Cu_xNi_9/Cu(001)$ trilayers is kept constant. The open triangles result from XMCD measurements [16], whereas the other data result from FMR experiments. The left-hand y-axis corresponds to the Cu/Ni/Cu/Ni system and the right-hand axis to the Ni/Cu/Co trilayers. Note that XMCD cannot deduce the absolute value of J_{inter}, so that in [16] a simple mean-field approach was used to obtain absolute values of J_{inter}. This approach results in values which are too large by about two orders of magnitude so that it was necessary to scale the XMCD data in figure 18 on the y-axis to match the correct values obtained by FMR. Figure 18 shows that after this scaling the results from both techniques are in excellent agreement showing a clear oscillatory behaviour which, within the error bars, is the same for both systems. Upon using the two theoretically predicted oscillation periods of 2.56 and 5.88 ML as well as the theoretical phases for a Cu(001) spacer [5] (see also section 2.1), one ends up with the curve shown as a solid line. The curve shows a reasonable agreement with the experiment, once the amplitudes are scaled to match the experimental J_{inter}. Since only the spacer Fermi surface defines the periods and the spacer for both systems is Cu(001), one expects the period to be the same for both trilayer types, but interestingly also the phases for both periods are the same for the two cases. The amplitude of the oscillations, i.e. the coupling strength of the two systems, shows that for the $Ni_7Cu_xCo_2/Cu(001)$ trilayers the coupling strength is about a factor of three larger than in the case of $Cu_4Ni_8Cu_xNi_9/Cu_{(001)}$ trilayers. From a theoretical point of view still very little is known concerning the amplitude of the coupling. Thus, this example shows that the absolute FMR values are well suited to be compared to theoretical calculations.

6.1.2. Influence of the spacer roughness. The influence of the spacer roughness is calculated by simply averaging over the thickness fluctuations which are present in a rough spacer. One ends up with an effective value of J_{inter}. To perform this procedure there are conditions which have to be fulfilled. First, the lateral correlation length of the roughness ξ has to be large enough, so that the interlayer exchange coupling is locally well defined; typically this implies $\xi > d$, d being the spacer thickness. To discuss the influence of interface roughness $Cu_4Ni_8Cu_xNi_9/Cu(001)$ trilayers were prepared without annealing the spacer after the deposition. This results in interfaces described in section 4. An inspection of figures 9(a)

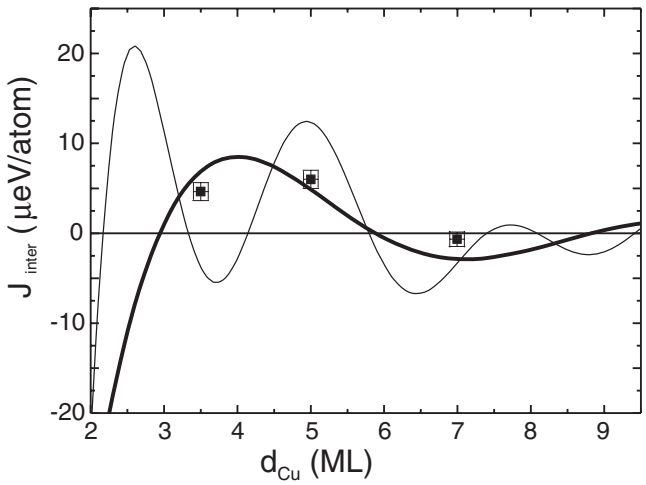

Figure 19. J_{inter} as a function of the spacer thickness d_{Cu} for trilayers having rough spacer layers. The thin solid curve corresponds to equation (1) using both periods; for the thick solid curve only the period of 5.88 ML was used.

and (c) shows that the lateral size of the pits on the non-annealed surfaces is on average at least in the order of 50 Å. The roughness of the non-annealed Cu spacer exhibits an even larger average island size. Thus, the lateral correlation length of the roughness is much larger than the spacer thicknesses which are investigated. Then, the effective value of J_{inter} is given by $\bar{J}_{inter} = \int P(d_{\mathrm{Cu}}) J_{inter}(d_{\mathrm{Cu}})\,\mathrm{d}\tau$ [40], where $P(d_{\mathrm{Cu}})$ is the distribution function of the roughness across the surface, $J_{inter}(d_{\mathrm{Cu}})$ is the expression for the coupling without roughness given by equation (1) and the integration has to be performed over the spacer thickness. As shown in [40], where the integral was solved for a Gaussian distribution $P(d_{\mathrm{Cu}})$, the effect of the interface roughness is essentially to attenuate the amplitude of the oscillatory behaviour of J_{inter}. If more than one oscillatory period is present, as for a Cu(001) spacer, the roughness mostly affects the period which is of the order of (or smaller than) the amplitude of the roughness or, in other words, the roughness acts as a low-pass filter. The results for $Cu_4Ni_8Cu_xNi_9$/Cu(001) trilayers with $x = 3.5, 5, 7$ are shown in figure 19 together with the theoretical curve already shown in figure 18 (thin solid curve). The thick solid curve is the theoretical curve, for which the short period has been omitted, i.e. only the longer period is used. The three points agree with the theoretical curve which proves the applicability of the model discussed in [40]. In particular, the trilayer with a spacer thickness of 3.5 ML shows ferromagnetic coupling, whereas the annealed one is antiferromagnetically coupled.

6.1.3. Influence of the temperature. The difference of J_{inter} from a Heisenberg exchange can be seen from the fact that it is strongly temperature dependent. Since J_{inter} measures the coupling strength it is all important to understand the mechanisms which lead to its temperature dependence. To conclude from experimental results it is a must to measure at more than only a few fixed temperatures. The two models introduced in section 2.1 will now be compared with our experimental results for $Ni_7Cu_xCo_2$/Cu(001) trilayers with $x = 5, 9$. Figure 18 shows that the trilayer with $x = 5$ is coupled ferromagnetically, whereas the trilayer with $x = 9$ is coupled antiferromagnetically. The complete temperature dependence of J_{inter} is displayed in the left-hand panel of figure 20 where J_{inter} is plotted as a function of $T^{3/2}$ for the two

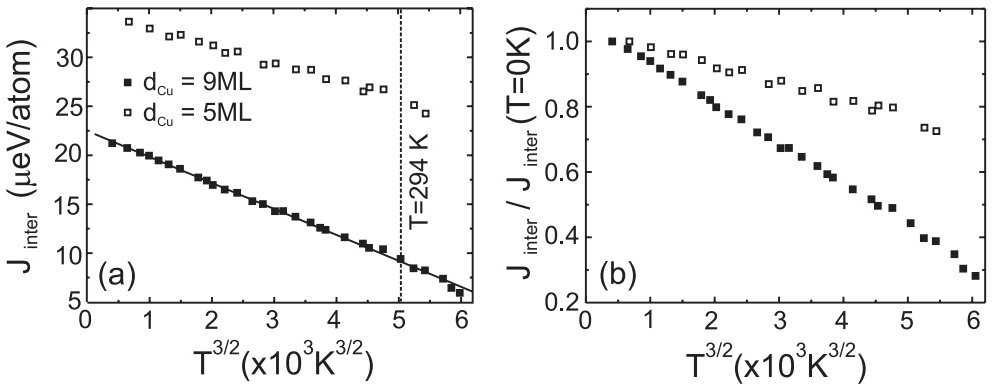

Figure 20. Temperature dependence of J_{inter} plotted as a function of $T^{3/2}$ for $Ni_7Cu_xCo_2/Cu(001)$ trilayers with $x = 5, 9$. In (a) absolute units and in (b) normalized values are shown.

cases. J_{inter} was deduced by the procedure described in section 5.2. In (a) absolute units and in (b) J_{inter} normalized to the extrapolated $T = 0$ K value are shown. For both trilayers J_{inter} has a linear dependence over a wide temperature range. This means that the dominating effect to the temperature dependence of J_{inter} results from the excitation of thermal spin waves at the interfaces of the ferromagnetic films which lead to a reduction of the coupling as the temperature increases. One should not conclude that the mechanism proposed by Bruno [5] is not present at all. The rounding of the Fermi surface with increasing temperature merely seems not to be of importance in the temperature range of interest. It was shown in [41] that a fit according to the Bruno model shows reasonable agreement only if unrealistic small values for v_F are used. The best fit is obtained for $v_F = 1.4 \times 10^7$ cm s^{-1} which is smaller by a factor of ten than the free electron value for Cu bulk ($v_F = 1.57 \times 10^8$ cm s^{-1}) and still smaller by a factor of five than realistic values determined experimentally by de Haas–van Alphen measurements yielding $v_F = 6.7 \times 10^7$ cm s^{-1} [42].

The model by Almeida *et al* [6] predicts that the coupling vanishes at the Curie temperature. Indeed, it was found in [41] that the coupling becomes at least very small. However, the model by Almeida *et al* also does not fully describe the temperature dependence as can be shown by comparing the dependences for two trilayers with different spacer thicknesses. One finds from figure 20 that the temperature dependence, despite being linear, is stronger for the trilayer with the larger spacer thickness, as can be seen best in (b). The Almeida model does not give an explanation for this behaviour, whereas the model by Bruno explicitly predicts this trend. This experimental finding thus shows that more theoretical work is needed to understand such a dependence on the spacer thickness. In particular, the origin of the constant a which is not discussed in [6] needs to be specified.

6.1.4. Influence of overlayer thickness. The theory used to describe the interlayer coupling effect as reviewed in section 2.1 predicts an oscillatory behaviour of the coupling as a function of J_{inter} which is clearly found experimentally. We will show in the following that an overlayer on top of a trilayer also influences J_{inter}. Usually such a capping layer is deposited on top of layered structures to protect them from oxidation. At first sight one might not expect any influence, but when a capping layer on top of the film structure is present, electron confinement can take place in the overlayer. This will subsequently change the net reflection coefficient of the topmost magnetic layer, and therefore the interlayer coupling should not only oscillate

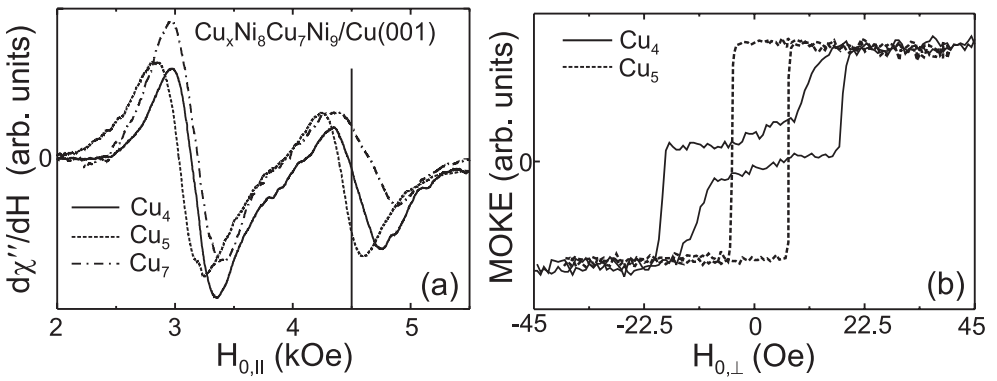

Figure 21. (a) FMR spectra for a $Cu_xNi_8Cu_7Ni_9/Cu(001)$ trilayer with different cap layer thicknesses of $x = 4, 5, 7$ ML. (b) Hysteresis loops for the same trilayer as shown in (a) obtained by polar Kerr-effect measurements for $x = 4, 5$ ML.

as a function of the spacer thickness, but also as a function of the overlayer thickness [14]. For all Cu/Ni/Cu/Ni/Cu(001) trilayers discussed up to now a Cu cap layer of 4 ML was used. Figure 21 shows the results of a measurement for a $Cu_xNi_8Cu_7Ni_9/Cu(001)$ trilayer for which the cap layer thickness was increased step by step from $x = 4$ to 7. The FMR spectrum of the trilayer capped with 4 ML (figure 21(a)) is plotted with the solid curve. The coupling of this system has already been discussed in figure 18. Instead of showing the whole signal of the bottom $Cu_7Ni_9/Cu(001)$ film, the resonance field of this film is indicated by a vertical line for better clarity. The analysis of this film yielded an antiferromagnetic coupling of $J_{inter} = -0.6$ μeV/atom. Upon adding only 1 ML of Cu on top of this trilayer the FMR spectrum changes to the one shown by the dashed line. Now one clearly sees that the acoustical mode is shifted to lower field values compared to the uncoupled system (vertical line). Therefore, the system is coupled ferromagnetically, i.e. J_{inter} has reversed its sign. Upon adding more layers of Cu, the system is again coupled antiferromagnetically as shown by the dash–dotted line. To support the FMR results, figure 21(b) shows hysteresis loops obtained from polar Kerr-effect measurements on the same trilayer system for cap layer thicknesses of 4 and 5 ML. For the 4 ML thick capping layer the occurrence of a flipping field of about 18 Oe indicates the antiferromagnetic coupling between the two Ni layers [43], whereas the squarelike loop for the 5 ML thick capping layer shows ferromagnetic coupling. Thus, consistent with the FMR result, the change from antiferromagnetic to ferromagnetic coupling is observed. After extracting the values of J_{inter} from FMR and plotting all the results as a function of the Cu overlayer thickness one ends up with figure 22. For antiferromagnetic coupling the values of J_{inter} can also be extracted from the flipping field in the Kerr-effect measurements as discussed in detail in [43]. The results are plotted as open squares together with the FMR values. Figure 22 shows a clear oscillatory behaviour. Compared to the amplitude of the oscillation as a function of the spacer thickness discussed in figure 18 the amplitude is rather small. Despite the large error bars in figure 22, the oscillatory character, i.e. the sign of the coupling, is determined unambiguously. The results show that especially for systems for which J_{inter} is close to zero a change of the overlayer thickness may lead to a change of sign in J_{inter} and that one has to be careful in comparing data obtained from weakly coupled samples having different cap layer thicknesses.

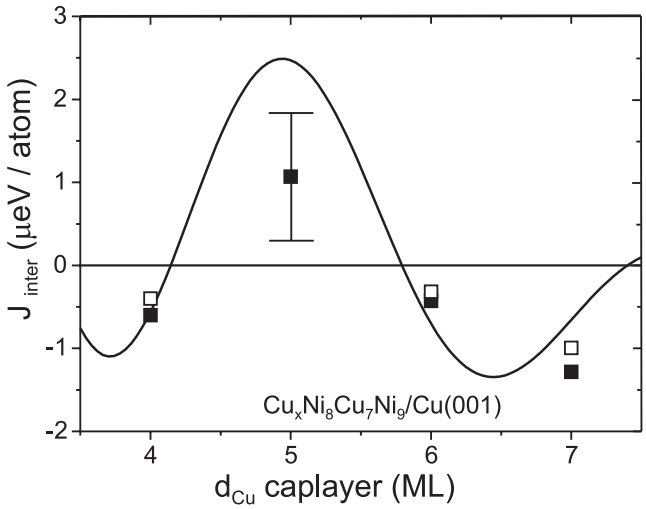

Figure 22. J_{inter} as a function of the Cu cap layer thickness measured by FMR (solid squares) and by MOKE (open squares). The solid curve corresponds to equation (1) with the amplitude scaled to the experiment.

6.1.5. Dependence on the microwave frequency. In the following the dispersion curve of the $Cu_4Ni_8Cu_5Ni_9/Cu(001)$ trilayer is discussed. The measurements made at a frequency of 9 GHz are extended by experiments using 4 GHz. The results, i.e. the measured H_{res}-values together with a fit according to equation (26), are plotted in figure 23. The data are best fitted using the values already obtained from the 9 GHz measurement discussed in section 5.2. Figure 23(a) shows the dispersion curve for the case where the external field is aligned within the film plane. The inset in (b) shows the spectrum taken at 4 GHz. As shown in section 5.2 this trilayer system exhibits an easy axis of magnetization *normal* to the film plane. Thus, the situation is different from the general example given in section 3.4, where a system having an in-plane easy axis was assumed. Again different regions are observed depending on the external field value. In (a) it can be seen that at low fields the dispersion is obviously different from the high field region. This behaviour is explained in (b), where the equilibrium angles $\theta^0_{1,2}$ of the two magnetizations are plotted as a function of H_0. At small fields the two magnetizations are not aligned parallel to each other. Thus, for the two resonances occurring at low fields at 4 GHz the magnetizations precess not about H_0, but rather about the internal field within the sample. In addition, both resonances are of optical character which is reflected in the smaller intensity compared to the acoustical mode located at the highest field of about 3 kOe. At 4 GHz only for the acoustical mode the two magnetization vectors are aligned parallel to each other during the precession. Again this is shown in (b), where starting from a field of 2.5 kOe both magnetizations are aligned parallel to each other. At 9 GHz only two resonances are observed as discussed in section 3.4. Both of them occur in the aligned regime, so that the clear identification of optical and acoustical modes is possible.

6.2. Analysis of the mode linewidth

In the last paragraph the influence of the interlayer exchange coupling on the resonance field H_{res} of the bilayer film has been discussed. Besides this an influence on the linewidth, i.e. on the damping properties, arising from the presence of the second magnetic layer can be seen.

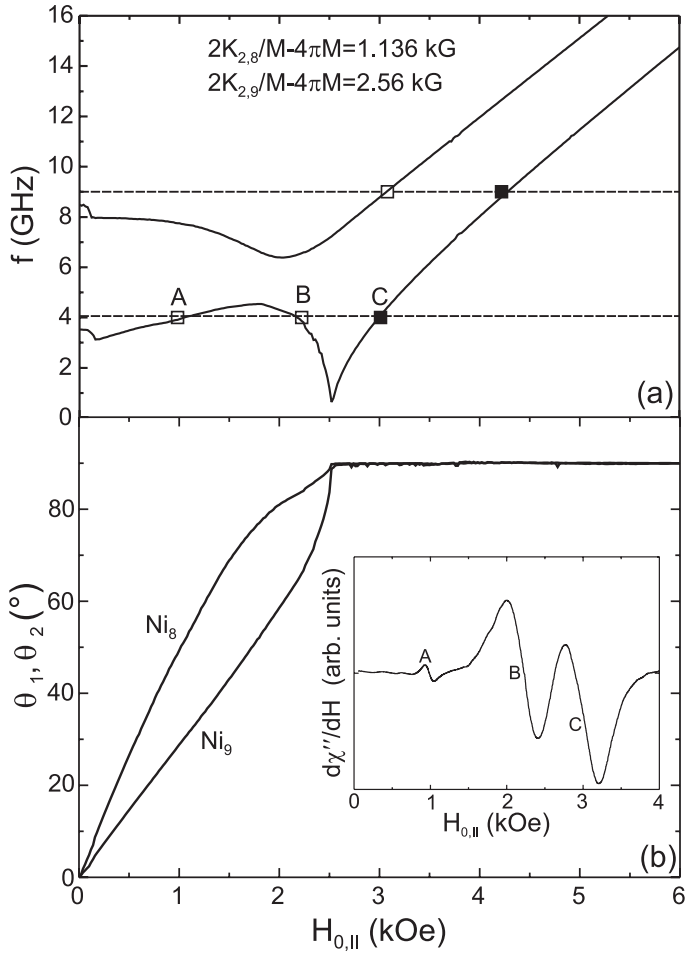

Figure 23. Calculated dependences of (a) frequency for the optical and acoustical mode and (b) the equilibrium angles $\theta^0_{1,2}$ of the two magnetizations as a function of the external field which is applied in the film plane. The points in (a) are the measured resonance fields for $f = 4, 9$ GHz. The inset in (b) shows the spectrum obtained at $f = 4$ GHz.

Before discussing the experimental results, a few words concerning the most frequently used definitions of the FMR linewidth ΔH_{pp} are summarized. In the literature several forms of the damping term within the LL equation have been proposed. The LL term, λ being the adjustable parameter, has the form $\frac{\lambda}{M^2}\vec{M} \times (\vec{M} \times \vec{H}^{eff})$. The vector $\vec{M} \times (\vec{M} \times \vec{H}^{eff})$ is perpendicular to $\vec{M}$ and directed towards $\vec{H}^{eff}$. Another frequently used form is the Gilbert damping $\frac{G}{M}\vec{M} \times \frac{\mathrm{d}\vec{M}}{\mathrm{d}t}$. In the following the Gilbert form will be used, but for small values of G, i.e. when terms in G^2 can be neglected, both expressions are equivalent [46]. The damping is added as effective field to the LL equation of motion [18]. Then, via G or λ the linewidth can be adjusted to match the experiment. However, such a phenomenological inclusion of damping does not give a microscopic insight into the origins of magnetic relaxation. Since even in single magnetic films there is still an ongoing discussion about the mechanisms of the observed ΔH_{pp}-value, it seems to be even more complicated to understand the linewidth observed in multilayers. We will thus show the results without the aim of giving a rigid explanation. Nevertheless, the *in*

situ approach allows for a step by step investigation providing a tool to look for sources of spin wave relaxation.

6.2.1. Influence of the coupling field. To discuss the influence of the coupling on the linewidth, the measured values for ΔH_{pp} taken from $Cu_4Ni_8Cu_xNi_9/Cu(001)$ trilayers with different spacer thicknesses are shown in figure 24. Two observations are made.

(i) The linewidth of both optical and acoustical modes has the tendency to increase as a function of spacer thickness. This effect may be understood as inhomogeneous broadening coming from variations in the spacer roughness which consequently produce a small lateral variation in the coupling field leading to slightly different resonance fields. As a result a broadening occurs from the overlap of the signals from different positions on the sample. This scenario is also supported by the observation that the increase of ΔH_{pp} in trilayers with non-annealed spacer layers was found to be larger.
(ii) Another effect which appears in figure 24 is that there is a difference in the broadening between optical and acoustical modes. The optical mode is always more broadened with respect to the single-layer resonance.

Moreover, as figure 24 reveals, this effect scales with the coupling strength given by J_{inter} in figure 18. For large values of J_{inter}, e.g. for spacer thicknesses of 2 and 5 ML, the difference of optical and acoustical mode broadening is largest. In contrast, for small coupling the ΔH_{pp}-values for optical and acoustical modes are also close to each other, e.g. for 7 ML spacer thickness. Thus, there seems to be an intrinsic mechanism that broadens the optical mode much more than the acoustical one. One possible explanation of this effect is given in the recent paper by Urban *et al* [44] which uses a theoretical model proposed by Berger [45]. There, it was shown that the magnetic layers in trilayer systems acquire an additional interface damping of Gilbert type. This damping results from the transfer of angular momentum between the magnetic films by the itinerant electrons entering the ferromagnetic layers through the spacer and leads to additional relaxation torques, because the electrons cannot immediately accommodate the direction of the precessing magnetization. It is not clear why the optical mode, i.e. the mode where the two magnetizations precess out of phase, seems to be more affected. Thus, more investigations are needed to understand this finding.

6.2.2. Temperature dependence. Figure 25 shows the experimentally observed temperature dependence of the linewidth for $Cu_4Ni_8Cu_xNi_9/Cu(001)$ trilayers with spacer thicknesses of $x = 5$ and 12 together with the linewidth found in the bottom $Cu_xNi_9/Cu(001)$ films before the deposition of the topmost Ni layers. The single films show almost the same linewidth indicating the good reproducibility which is achieved by our *in situ* growth. After the evaporation of the topmost films the acoustical mode always has a ΔH_{pp} which is larger by about 50 G than the one found in the single films. This may arise from a small inhomogeneous contribution due to the roughness of the spacer which even after annealing cannot absolutely be removed as discussed in the previous section. In addition, again the optical mode exhibits an even larger linewidth. Now we come to the temperature dependence. First, we note that the trilayer with a Cu spacer of 5 ML was found to have quite a strong coupling as figure 18 reveals. The coupling for the trilayer having a Cu spacer thickness of 12 ML on the other hand is very small, i.e. the position of the acoustical mode in the trilayer was found to be nearly at the same position as the single resonance observed from the bottom film only. Starting from the temperature dependence of ΔH_{pp} for the optical modes one sees that at the position where one expects the T_C of the topmost film the linewidth suddenly increases, being steeper for the

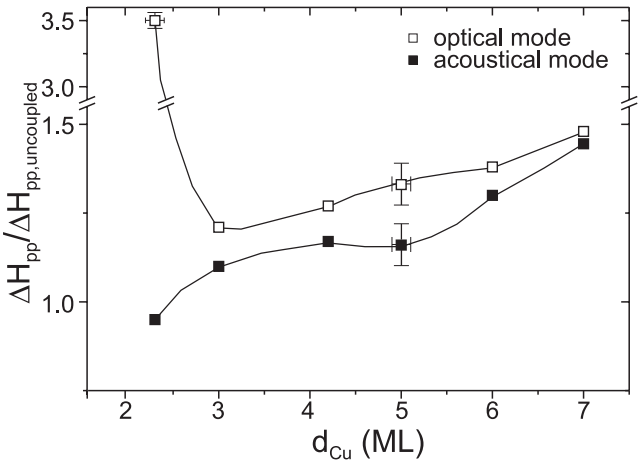

Figure 24. Linewidth normalized to the one found for the individual Cu capped Ni films as a function of spacer thickness for acoustical and optical modes in $Cu_4Ni_8Cu_xNi_9/Cu(001)$ trilayers. The curve serves as a guide to the eye.

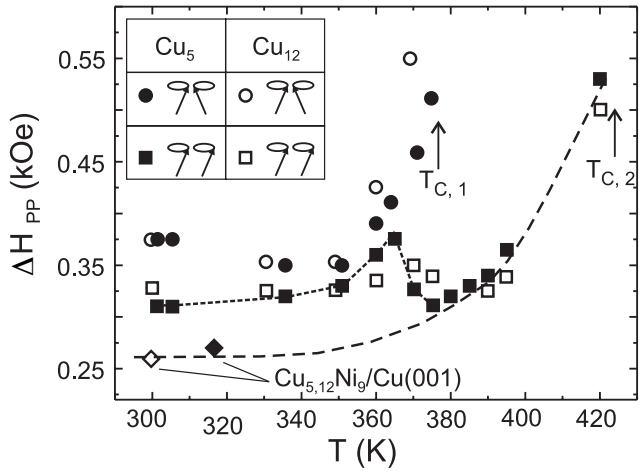

Figure 25. Linewidth as a function of temperature for acoustical and optical modes in two $Cu_4Ni_8Cu_xNi_9/Cu(001)$ trilayers with $x = 5$ and 12.

$Cu_4Ni_8Cu_{12}Ni_9/Cu(001)$ trilayer. Such an effect is well known to arise from spin fluctuations at the Curie point [46, 47]. In [48] it was shown that the presence of a coupling field may influence the magnetic properties of the two films. It was found that for reasonable values of J_{inter} the influence of the coupling field on the magnetic films can be explained only if the magnetic fluctuations in the 2D films are properly taken into account, i.e. a mean-field approach does not account for the effects. This means that the most important influence of the coupling field is to suppress the spin fluctuations. The coupling is smaller for the trilayer with a Cu spacer layer of 12 ML. Thus, the steeper increase shown in figure 25 stems from the stronger spin fluctuations. Another observation in figure 25 is that at the point where the optical mode intensity increases a peak is observed for ΔH_{pp} of the acoustical mode which is larger for the $Cu_4Ni_8Cu_5Ni_9/Cu(001)$ trilayer. This shows that the spin fluctuations in the topmost film also influence the bottom one, so that one cannot, in principle, treat the fluctuations independently.

7. Summary

We have shown that UHV *in situ* FMR is a powerful tool to study coupled ferromagnetic films, since a step by step investigation allows us to directly compare the same system before and after the coupling is activated via the deposition of the second magnetic layer. To analyse the spectra we have calculated the full FMR signal for the complete out-of-plane angular range. Good agreement was found for the resonance fields and intensities. Further, the calculation allows us to extract the coupling strength in absolute energy units for ferro- as well as antiferromagnetic coupling. Via the *in situ* approach this can be done by analysing the field shift of the modes in the coupled system with respect to the single film and this allows us to deduce the coupling even if only one mode is observed. Moreover, it opens a direct way to deduce the coupling, because the influence of the anisotropies and the coupling can be separated. Our experiments reveal that

(i) the coupling shows an oscillatory behaviour and
(ii) it is strongly temperature dependent. The most important source of this dependence arises from the temperature dependent disorder of the magnetic moments at the interface to the spacer due to thermally activated spin waves.
(iii) The spacer roughness which was quantitatively investigated via STM has a dramatic influence on J_{inter}. It strongly suppresses the small period of the oscillatory coupling.
(iv) The effect of an overlayer is discussed. We have shown that such a layer, which usually is deposited for an 'inert' protection, can even change the sign of the coupling.
(v) The dispersion relation $f(H_0)$ of the trilayers was discussed together with results from *in situ* measurements at frequencies of 4 and 9 GHz.
(vi) Finally, we have presented results which show that the linewidth is influenced by the presence of the coupling field, leading to an extra damping.

In addition, the temperature dependent linewidth of coupled layers directly reflects the interaction between the films.

Acknowledgments

P Poulopoulos, D L Mills, P Weinberger, K Heinz, B Heinrich and P Bruno are acknowledged for fruitful discussions. E Kosubek, A Anisimov and C Rüdt are acknowledged for assistance during the FMR measurements and C Sorg, R Nünthel and H Wende for proof reading the manuscript. This work was supported by the DFG, Sfb 290 and BMBF(05KS1 KEB4).

References

[1] Grünberg P, Schreiber R, Pang Y, Brodsky M B and Sowers H 1986 *Phys. Rev. Lett.* **57** 2442
[2] Farle M 1998 *Rep. Prog. Phys.* **61** 755
[3] Almeida N S and Mills D L 1988 *Phys. Rev.* B **38** 6698
[4] Lindner J, Kollonitsch Z, Kosubek E, Farle M and Baberschke K 2001 *Phys. Rev.* B **63** 094413
[5] Bruno P 1995 *Phys. Rev.* B **52** 411
[6] Almeida N S, Mills D L and Teitelman M 1995 *Phys. Rev. Lett.* **75** 733
[7] Drchal V, Kudrnovský J, Bruno P, Turek I, Dederichs P H and Weinberger P 1999 *Phys. Rev.* B **60** 9588
[8] Ruderman M A and Kittel C 1954 *Phys. Rev.* **96** 99
[9] Kasuya T 1956 *Prog. Theor. Phys.* **16** 45
[10] Yosida K 1957 *Phys. Rev.* **106** 893
[11] Bruno P 1992 *J. Magn. Magn. Mater.* **116** L13
[12] Edwards D M, Mathon J, Muniz R B and Phan M S 1991 *Phys. Rev. Lett.* **67** 493
[13] Stiles M D 1993 *Phys. Rev.* B **48** 7238

[14] Bruno P 1999 *J. Phys.: Condens. Matter* **11** 9403
[15] Ney A, Poulopoulos P, Farle M and Baberschke K 2000 *Phys. Rev.* B **62** 11336
[16] Ney A, Wilhelm F, Farle M, Poulopoulos P, Srivastava P and Baberschke K 1999 *Phys. Rev.* B **59** R3938
[17] Krebs J J, Lubitz P, Chaiken A and Prinz G A 1989 *Phys. Rev. Lett.* **63** 1645
[18] Heinrich B and Cochran J F 1993 *Adv. Phys.* **42** 523
[19] Grünberg P A 1985 *Prog. Surf. Sci.* **18** 1
[20] Layadi A and Artman J O 1990 *J. Magn. Magn. Mater.* **92** 143
[21] Wigen P E, Zhang Z, Zhou L, Ye M and Cowen J A 1993 *J. Appl. Phys.* **73** 6338
[22] Zhang Z, Zhou L, Wigen P E and Ounadjela K 1994 *Phys. Rev. Lett.* **73** 336
Zhang Z, Zhou L, Wigen P E and Ounadjela K 1994 *Phys. Rev.* B **50** 6094
[23] Rezende S M, Chesman C, Lucena M A, Azevedo A, de Aguiar F M and Parkin S S P 1998 *J. Appl. Phys.* **84** 958
[24] Anisimov A N, Farle M, Poulopoulos P, Platow W, Baberschke K, Isberg P, Wäppling R, Niklasson A M N and Eriksson O 1999 *Phys. Rev. Lett.* **82** 2390
[25] Platow W, Anisimov A N, Dunifer G L, Farle M and Baberschke K 1998 *Phys. Rev.* B **58** 5611
[26] Smit J and Beljers H G 1955 *Philips Res. Rep.* **10** 113
[27] Kittel C 1947 *Phys. Rev.* **71** 270
Kittel C 1948 *Phys. Rev.* **73** 155
Kittel C 1949 *Phys. Rev.* **76** 743
[28] Ritter M, Stindtmann M, Farle and Baberschke K 1996 *Surf. Sci.* **348** 243
[29] Heinz K, Müller S and Hammer L 1999 *J. Phys.: Condens. Matter* **11** 9437
[30] de Miguel J J, Cebollada A, Gallego J M, Miranda R, Schneider C M, Schuster P and Kirschner J 1991 *J. Magn. Magn. Mater.* **93** 1
[31] Nouvertné F, May U, Rampe A, Gruyters M, Korte U, Berndt R and Guentherodt G 1999 *Surf. Sci.* **436** L653
Nouvertné F, May U, Bamming M, Rampe A, Korte U, Guentherodt G, Pentcheva R and Scheffler M 1999 *Phys. Rev.* B **60** 14382
[32] Fassbender J, Allenspach R and Dürig U 1997 *Surf. Sci.* **383** L742
[33] Lindner J, Poulopoulos P, Wilhelm F, Scherz A, Farle M and Baberschke K 2000 *Phys. Rev.* B **62** 10431
[34] Wilhelm F, Bovensiepen U, Scherz A, Poulopoulos P, Ney A, Wende H, Ceballos G and Baberschke K 2000 *J. Magn. Magn. Mater.* **222** 163
[35] Poulopoulos P and Baberschke K 1999 *J. Phys.: Condens. Matter* **11** 9495
[36] Baberschke K 2001 *Anisotropy in Magnetism (Springer Lecture Notes in Physics vol 580)* (Berlin: Springer) pp 27–45
[37] Bovensiepen U, Poulopoulos P, Platow W, Farle M and Baberschke K 1999 *J. Magn. Magn. Mater.* **192** L386
[38] Poulopoulos P, Jensen P J, Ney A, Lindner J and Baberschke K 2002 *Phys. Rev.* B **65** 064431
[39] van Dijken S, Vollmer R, Poelsema B and Kirschner J 2000 *J. Magn. Magn. Mater.* **210** 316
[40] Levy P M, Maekawa S and Bruno P 1998 *Phys. Rev.* B **58** 5588
[41] Lindner J, Rüdt C, Kosubek E, Poulopoulos P, Baberschke K, Blomquist P, Wäppling R and Mills D L 2002 *Phys. Rev. Lett.* **88** 167206
[42] Persat N and Dinia A 1997 *Phys. Rev.* B **56** 2676
[43] Dieny B, Gavigan J P and Rebouillat J P 1990 *J. Phys.: Condens. Matter* **2** 159
Dieny B, Gavigan J P and Rebouillat J P 1990 *J. Phys.: Condens. Matter* **2** 187
[44] Urban R, Woltersdorf G and Heinrich B 2001 *Phys. Rev. Lett.* **87** 217204
[45] Berger L 1996 *Phys. Rev.* B **54** 9353
[46] Vonsovski S V 1966 *Ferromagnetic Resonance* (New York: Pergamon)
[47] Li Y and Baberschke K 1992 *Phys. Rev. Lett.* **68** 1208
[48] Jensen P J, Bennemann K H, Poulopoulos P, Farle M, Wilhelm F and Baberschke K 1999 *Phys. Rev.* B **60** R14994